

DEFT: Differentiable Branched Discrete Elastic Rods for Modeling Furcated DLOs in Real-Time

Yizhou Chen Xiaoyue Wu Yeheng Zong Anran Li Yuzhen Chen
Julie Wu Bohao Zhang Ram Vasudevan

Department of Robotics, University of Michigan, Ann Arbor, MI 48109, United States

{yizhouch, wxylna, yehengz, anranli, yuzhenc, jwuxx, jimzhang, ramv}@umich.edu

Abstract—Autonomous wire harness assembly requires robots to manipulate complex branched cables with high precision and reliability. A key challenge in automating this process is predicting how these flexible and branched structures behave under manipulation. Without accurate predictions, it is difficult for robots to reliably plan or execute assembly operations. While existing research has made progress in modeling single-threaded Deformable Linear Objects (DLOs), extending these approaches to Branched Deformable Linear Objects (BDLOs) presents fundamental challenges. The junction points in BDLOs create complex force interactions and strain propagation patterns that cannot be adequately captured by simply connecting multiple single-DLO models. To address these challenges, this paper presents Differentiable discrete branched Elastic rods for modeling Furcated DLOs in real-Time (DEFT), a novel framework that combines a differentiable physics-based model with a learning framework to: 1) accurately model BDLO dynamics, including dynamic propagation at junction points and grasping in the middle of a BDLO, 2) achieve efficient computation for real-time inference, and 3) enable planning to demonstrate dexterous BDLO manipulation. A comprehensive series of real-world experiments demonstrates DEFT’s efficacy in terms of accuracy, computational speed, and generalizability compared to state-of-the-art alternatives.

I. INTRODUCTION

The automation of wire harness assembly represents a critical challenge in manufacturing, particularly in the automotive and aerospace industries where complex, branched cable systems are essential components. These assemblies require robots to manipulate Branched Deformable Linear Objects (BDLOs) with precision over extended periods (≥ 5 s) [1, 2, 3], a task that remains largely unautomated due to the objects’ complex nonlinear dynamics. While accurate prediction of BDLO behavior is possible through computationally intensive models, real-time manipulation demands rapid computation. Further complicating matters, practical assembly environments often involve occlusions that prevent perception systems from reliably estimating the full BDLO configuration.

Existing approaches to modeling BDLOs [4, 5, 6, 7] have focused primarily on computer graphics applications, prioritizing visual plausibility over physical accuracy. These models typically require extensive manual parameter tuning and make impractical assumptions about perfect state observation—limitations that render them unsuitable for robotic manipulation tasks. Recent advances in modeling single Deformable Linear Objects (DLOs) [8, 9, 10, 11, 12] have shown

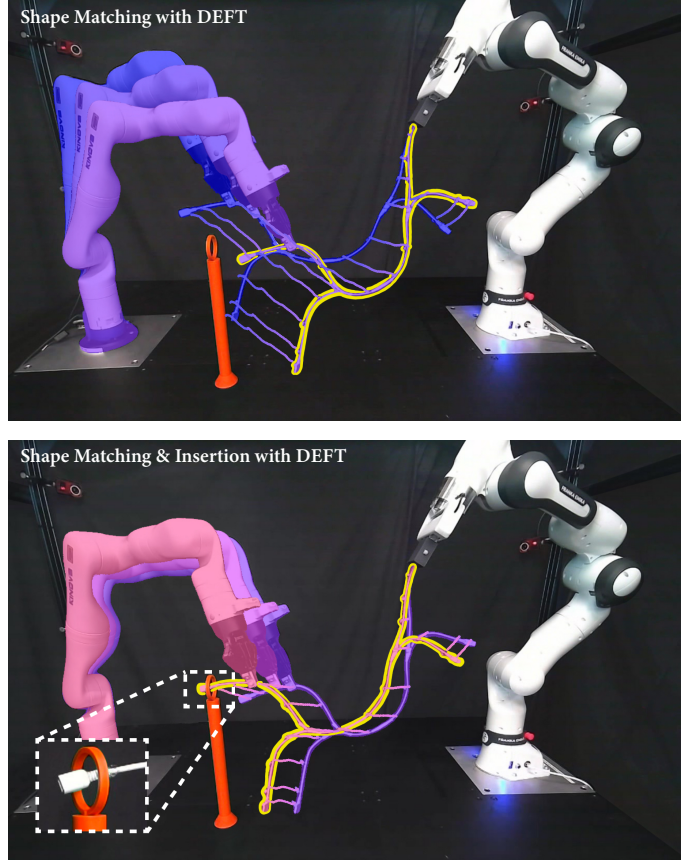


Fig. 1: This paper introduces DEFT, a novel framework that combines a differentiable physics-based model with a learning-based approach to accurately model and predict the dynamic behavior of Branched Deformable Linear Objects (BDLOs) in real time. As this paper illustrates, this model can be used in concert with a motion planning algorithm to autonomously manipulate BDLOs. The figures above illustrate how DEFT can be used to autonomously complete a wire insertion task. **Top:** The system first plans a shape-matching motion, transitioning the BDLO from its **initial** configuration to the target shape (contoured with **yellow**), which serves as an intermediate waypoint. **Bottom:** Starting from the intermediate configuration, the system performs thread insertion, guiding the BDLO into the **target hole** while also matching the target shape. Notably, DEFT predicts the state of the wire recursively without relying on ground truth or perception data at any point in the process.

promise, but the extension to branched structures introduces fundamental new challenges. When a robot manipulates one branch of a wire harness, the forces and deformations propa-

gate through junction points to affect all connected branches. This coupling between branches, combined with the need for flexible grasp locations and real-time computation, makes BDLO manipulation significantly more complex than handling single DLOs.

To address these challenges, this paper introduces Differentiable Branched Discrete Elastic Rods for Modeling Furcated DLOs in Real-Time (DEFT). This framework introduces a novel junction coupling approach that accurately models dynamic propagation between parent and child branches while maintaining real-time performance. As this paper illustrates through real-world evaluations, DEFT enables three essential wire harness assembly tasks: 3D shape matching, multi-thread grasp, and precise thread grasping and insertion. The contributions of this paper are four-fold:

- 1) A novel differentiable BDLO model that accurately captures how dynamics propagate through wire harness junction points thereby enabling model parameters to be efficiently identified via experimental observation;
- 2) A computational representation that enables efficient inference and model parameter learning through parallel programming in concert with analytical gradients;
- 3) A specialized Graph Neural Network (GNN) architecture for BDLO residual learning, which can compensate for numerical integration errors that arise over long time horizon prediction;
- 4) A comprehensive experimental validation demonstrating DEFT's superior performance in accuracy, speed, and sampling efficiency compared to existing approaches, including integration into a motion planning framework for real-world manipulation tasks.

The framework is implemented in PyTorch for seamless integration with deep learning workflows, and represents, to the best of our knowledge, the first quantitative investigation of BDLO modeling and manipulation in real-world settings. The results demonstrate that DEFT enables reliable autonomous manipulation of complex wire harnesses, addressing a significant challenge in manufacturing automation. Upon acceptance the code associated with this paper will be made publically available.

II. RELATED WORK

Effective BDLO modeling requires three critical capabilities: real-time prediction, accurate 3D simulation, and efficient model parameter learning. Real-time prediction capability is essential for robotic manipulation tasks, where quick decision-making can mean the difference between successful and failed object handling. Three-dimensional accuracy ensures the model can capture the complex spatial deformations that BDLOs undergo during manipulation, including twisting, bending, and branch interactions. Efficient parameter learning enables models to automatically adapt to different materials and configurations through data-driven optimization, reducing both computational overhead and the need for extensive training data. This section reviews relevant approaches in modeling

BDLOs and single DLOs while considering each of these criteria.

A. DLOs Modeling

Approaches to modeling DLOs have evolved from purely physics-based methods toward more sophisticated learning-based frameworks that balance between the three aforementioned key capabilities.

Physics-based approaches implement different mathematical frameworks to model physical behavior. Mass-spring systems represent objects as networks of point masses connected by springs, computing forces and accelerations to simulate movement [13, 14, 15]. Position-Based Dynamics (PBD) directly manipulates vertex positions to satisfy physical constraints, avoiding expensive force calculations [10, 16, 9]. Finite Element Methods (FEM) divide objects into discrete elements and solve partial differential equations to compute deformations [17, 18, 19]. Discrete Elastic Rods (DER) models represent objects as centerline curves with material frames, enabling explicit modeling of bending and twisting [16, 20, 21, 22]. Unfortunately each of these methods has limitations: mass-spring systems describe the rigidity of wires by introducing large spring stiffness which can make prediction numerically unstable; PBD models struggle with parameter learning because they assume that the system is quasi-static; FEM methods are computationally intensive; and DER models lack differentiable expressions for their model parameters, making efficient parameter optimization challenging.

Learning-based modeling approaches use data-driven techniques to predict deformation behavior. Methods such as Graph Neural Networks (GNN) process vertex-level spatial information [12], while Bi-LSTM models capture temporal dependencies in deformation sequences [11]. These approaches excel at real-time prediction through efficient computation and support straightforward parameter learning through standard optimization techniques. However, they struggle with 3D accuracy, particularly in capturing the complex dynamic deformations characteristic of real-world manipulation.

Recent work has explored hybrid approaches that combine learning with physics-based modeling. This is exemplified by DEFORM [8] which constructs a novel differentiable DER model and combines it with a neural network-based residual learning approach to account for numerical integration errors during prediction. This hybrid approach achieves both real-time performance and 3D accuracy while enabling efficient parameter learning through end-to-end differentiability.

Despite DEFORM's advances in DLO modeling, it faces three significant limitations when extended to BDLO applications. First, DEFORM's modeling framework does not address the dynamics of branched structures, particularly the propagation of stretching, twisting, and bending forces at junction points. Second, DEFORM's manipulation framework assumes fixed clamping points at the object ends, following conventional DLO literature. This assumption restricts its applicability to more sophisticated manipulation tasks, such as thread insertion, which require grasping at multiple points

along the object's length. Third, DEFORM's computational approach presents efficiency challenges for BDLO simulation. Its sequential processing of individual branches would result in linear computational time increases as branches are added. Furthermore, its bi-level optimization framework, while enabling learning from real-world data, relies on numerical gradients that can lead to slow convergence and optimization instability.

B. BDLOs Modeling

Existing BDLO modeling approaches adapt various physical simulation frameworks to handle branched structures. FEM-based methods extend traditional finite element analysis by treating branches as connected elastic elements [23]. While these methods excel in 3D accuracy and enable efficient parameter learning through gradient-based optimization, their computational requirements preclude real-time prediction. DER-based approaches introduce rigid-body constraints at junctions to ensure proper alignment of attached segments [4], achieving real-time performance and reasonable 3D accuracy but struggling with parameter learning due to their fixed parameter structure. Quasi-static methods like ASMC enforce geometric constraints while assuming static equilibrium conditions [5], offering real-time performance, but sacrificing 3D accuracy by overlooking dynamic effects that can make parameter learning challenging.

To address these challenges, DEFT introduces a novel differentiable framework specifically designed for BDLOs. Through a specialized GNN architecture for branched structures, DEFT achieves all three critical capabilities: real-time performance, 3D accuracy, and efficient parameter learning. This enables DEFT to adapt to various materials and configurations while maintaining the speed and accuracy necessary for practical robotic manipulation tasks.

III. PRELIMINARIES

This section introduces the key components involved in modeling DLOs. It then summarizes the primary contributions of DEFORM and describes the challenges of adapting it to BDLO modeling.

A. Deformable Linear Object (DLO) Model

To model a DLO, we represent it as an indexed set of n vertices at each time instance. The ground truth location of vertex i at time t is denoted by $\mathbf{x}_t^i \in \mathbb{R}^3$, and the set of all n vertices is denoted by \mathbf{X}_t . A segment, or edge, in the DLO is the line between successive vertices, $\mathbf{e}_t^i = \mathbf{x}_t^{i+1} - \mathbf{x}_t^i$. Let \mathbf{E}_t correspond to the set of all edges at time t . Let $\mathbf{M}_i \in \mathbb{R}^{3 \times 3}$ denote the mass matrix of vertex i . The velocity of the vertices of the DLO is approximated by $\mathbf{V}_t = (\mathbf{X}_t - \mathbf{X}_{t-1})/\Delta t$, where Δt is the time step between frames. Note that \mathbf{V}_t is an approximation of the actual velocities. We distinguish between ground truth elements and predicted elements by using the circumflex symbol (e.g., $\hat{\mathbf{X}}_t$ is the ground truth set of vertices at time t , and $\hat{\mathbf{X}}_t$ is the predicted set of vertices at time t).

B. Modeling DLOs with DEFORM

1) *Discrete Elatic Rods (DER)*: DEFORM builds upon DER theory to model three distinct deformation modes of DLOs: bending, twisting, and stretching. DER theory models DLOs using two key families of coordinate frames. First, it introduces Bishop Frames, which provide a twist-free reference state along the centerline of the rod. The Bishop Frame only rotates to follow the curve's geometry, providing a relaxed baseline configuration for the DLO. Second, the theory employs Material Frames, which describe the actual physical deformation of the rod. Material Frames can be expressed relative to the Bishop Frames through a single angle whose rate of change represents the physical twist of the DLO. To describe the twist of the DLO, DER theory assumes that the angle of the Material Frame with respect to the Bishop Frame is one that minimizes the potential energy of the DLO. We briefly summarize DER theory in this section, but a longer introduction can be found here [24].

Bishop Frame: The Bishop Frame at edge i is made up of three axes $\{\mathbf{t}^i, \mathbf{b}_1^i, \mathbf{b}_2^i\}$. We next formally define each axis of the Bishop Frame. First, $\mathbf{t}^i \in \mathbb{R}^3$ is the unit tangent along edge i which is defined as $\mathbf{t}^i = (\mathbf{x}^{i+1} - \mathbf{x}^i)/\|\mathbf{x}^{i+1} - \mathbf{x}^i\|_2$. The vector $\mathbf{b}_1^i \in \mathbb{R}^3$ is defined iteratively by applying a rotation matrix to the previous Bishop frame: $\mathbf{b}_1^i = \mathbf{R}^i \cdot \mathbf{b}_1^{i-1}$. The rotation matrix $\mathbf{R}^i \in \mathbb{R}^{3 \times 3}$ satisfies the following conditions

$$\mathbf{t}^i = \mathbf{R}^i \cdot \mathbf{t}^{i-1} \quad (1)$$

$$\mathbf{t}^{i-1} \times \mathbf{t}^i = \mathbf{R}^i \cdot (\mathbf{t}^{i-1} \times \mathbf{t}^i). \quad (2)$$

The first condition ensures that the tangent vector of the DLO at each subsequent edge can be described using the rotation matrix and the tangent vector at the previous edge. Though we do not prove it here, the second condition ensures that the rotation between successive Bishop Frames is minimal while moving along the DLO. In particular, this latter condition ensures that there is no twist about the subsequent tangent vectors at each edge of the DLO. Finally, $\mathbf{b}_2^i := \mathbf{t}^i \times \mathbf{b}_1^i$, which ensures that \mathbf{b}_2^i is orthogonal to \mathbf{t}^i and \mathbf{b}_1^i .

Material Frame: Subsequently, DER theory introduces Material Frames that are made up of three axes $\{\mathbf{t}^i, \mathbf{m}_1^i, \mathbf{m}_2^i\}$. These Material Frames are generated by rotating the Bishop frame about the tangent vector by a scalar θ^i , i.e., $\mathbf{m}_1^i, \mathbf{m}_2^i$ are defined as

$$\mathbf{m}_1^i = \mathbf{b}_1^i \cos \theta^i + \mathbf{b}_2^i \sin \theta^i \quad (3)$$

$$\mathbf{m}_2^i = -\mathbf{b}_1^i \sin \theta^i + \mathbf{b}_2^i \cos \theta^i \quad (4)$$

An illustration of the frames can be found in Figure 2.

Equations of Motion: Let $\Gamma(\mathbf{X}_t, \theta_t)$ denote the set of all $n - 1$ Material Frames at time t . Let α represent the vector of material properties for each vertex of the DLO (i.e., mass, bending modulus, and twisting modulus) [4, Section 4.2]. Using these definitions, one can compute the potential energy of the DLO arising from bending and twisting which we denote by $P(\Gamma(\mathbf{X}_t, \theta_t), \alpha)$. DER theory assumes that the DLO reaches an equilibrium state between each simulation

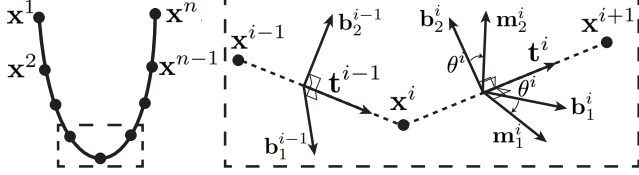


Fig. 2: An illustration of DER coordinate frames.

time step to obtain the optimal θ_t^* :

$$\theta_t^*(\mathbf{X}_t, \alpha) = \arg \min_{\theta_t} P(\Gamma(\mathbf{X}_t, \theta_t), \alpha) \quad (5)$$

Once $\theta_t^*(\mathbf{X}_t, \alpha)$ is derived, the restorative force during deformation is given by the negative gradient of the potential energy with respect to the vertices. Consequently, the equation of motion for the DLO is:

$$M\ddot{\mathbf{X}}_t = -\frac{\partial P(\Gamma(\mathbf{X}_t, \theta_t^*(\mathbf{X}_t, \alpha)), \alpha)}{\partial \mathbf{X}_t} \quad (6)$$

One can numerically integrate this formula to predict the velocity and position by applying the Semi-Implicit Euler method:

$$\hat{\mathbf{V}}_{t+1} = \hat{\mathbf{V}}_t - \Delta_t M^{-1} \frac{\partial P(\Gamma(\mathbf{X}_t, \theta_t^*(\mathbf{X}_t, \alpha)), \alpha)}{\partial \mathbf{X}_t}, \quad (7)$$

$$\hat{\mathbf{X}}_{t+1} = \hat{\mathbf{X}}_t + \Delta_t \hat{\mathbf{V}}_{t+1}, \quad (8)$$

where $\Delta_t > 0$ is a user specified time discretization.

2) *Differentiable Discrete Elastic Rods (DDER)*: Tuning the DER model parameters, α , to match real-world DLOs is non-trivial. To address this challenge, DEFORM introduces DDER, which enables the automatic tuning of DLO parameters using real-world data. Predicting $\hat{\mathbf{X}}_{t+1}$ with DDER through (7) and (8) involves solving an optimization problem as defined in (5). Consequently, minimizing the prediction loss requires solving a bi-level optimization problem at each time step t :

$$\min_{\alpha} \|\mathbf{X}_{t+1} - \hat{\mathbf{X}}_{t+1}(\theta_t^*)\|_2 \quad (9)$$

$$\theta_t^* = \arg \min_{\theta_t} P(\Gamma(\mathbf{X}_t, \theta_t), \alpha) \quad (10)$$

Note $\hat{\mathbf{X}}_{t+1}$ depends on the previously computed θ_t^* through (6), (7) and (8). To compute the gradient of (10) with respect to α , DEFORM employs solvers from Theseus [25], which use PyTorch's automatic differentiation [26]. As we illustrate via experiments in Section V, this can be a time-consuming process.

3) *Integration Method with Residual Learning*: To compensate for numerical errors that arise during numerical integration (8), DEFORM incorporates a learning-based framework into the integration method:

$$\hat{\mathbf{X}}_{t+1} = \hat{\mathbf{X}}_t + \Delta_t (\hat{\mathbf{V}}_{t+1} + \text{GNN}(\hat{\mathbf{X}}_t, \hat{\mathbf{V}}_t, \alpha)) \quad (11)$$

This structure builds on residual learning [27], grounding the neural network in physical laws while leveraging data-driven insights.

4) *Inextensibility Enforcement with Momentum Conservation*: After numerical integration, the DLO length may deviate from its initial value due to numerical errors, making it difficult to accurately model inextensible DLOs. A common physics-based approach [13, 14, 15] uses mass-spring systems to minimize this deviation, but this can result in stiff simulations and numerical instability. DEFORM addresses this by enforcing an inextensibility constraint while preserving momentum, leading to more accurate and stable simulation.

5) *Challenges of Extending DEFORM to BDLOs*: Though DEFORM can accurately simulate single-thread DLOs, it is unsuitable for BDLOs for several reasons. First, the definitions of Bishop and Material Frames do not generalize to BDLOs. To see why this is true, recall that at junctions in a BDLO there are several tangent vectors because there are more than two edges. As a result, satisfying (1) and (2) results in an overdetermined system which makes it impossible to find a rotation matrix \mathbf{R}^i that satisfies all constraints. Consequently, the Bishop and Material Frames cannot be defined at these junctions. An alternative to extend DEFORM to BDLOs is to simulate each branch individually using DEFORM. However, this requires repeatedly solving (5), which reduces computational efficiency. This is further complicated when trying to enforce inextensibility using the momentum conservation constraint. To address this, DEFT proposes a computational representation that supports parallel processing, enabling more efficient inference.

Second, relying on automatic differentiation to perform parameter tuning becomes computationally prohibitive when dealing with BDLOs. To address this limitation, DEFT utilizes the analytical gradients of $P(\Gamma(\mathbf{X}_t, \theta_t), \alpha)$ with respect to θ_t . Third, the GNN used by DEFORM during residual learning is tailored to single-strand DLOs. To address this limitation, DEFT introduces a specialized GNN Architecture for residual learning for BDLOs that can compensate for numerical integration errors over long horizon predictions.

IV. METHODOLOGY

Our objective is to model the dynamic behavior of a BDLO under robotic control. Traditional modeling approaches simplify the problem by assuming that the DLO's endpoints are each held by separate robot end-effectors [8, 28, 16, 10, 29, 30]. Although this assumption reduces complexity, it limits the potential for dexterous manipulation (e.g., inserting the middle of a BDLO into a plug). This work relaxes this assumption and considers scenarios where the BDLO is grasped at an intermediate point, rather than exclusively at its ends.

This section introduces the key components of BDLO modeling and overviews the various components of DEFT, which are illustrated in Figure 3. The key components of DEFT are: 1) analytical gradients to accelerate the optimization procedure used to solve (5); 2) a GNN architecture tailored for residual learning in BDLO simulations; 3) an inextensible constraint formulation that enables the propagation of dynamics at the junction between branches while conserving momentum, which improves the numerical stability of the

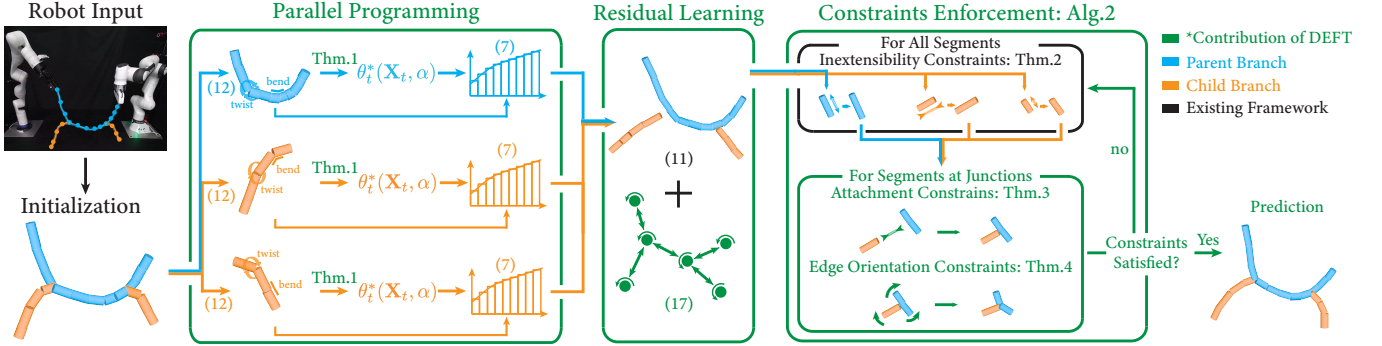


Fig. 3: Algorithm Overview of DEFT. In the initialization stage (Section IV-A), DEFT begins by separating the BDLO into a parent DLO and one or more children DLOs. Each DLO is discretized into vertices and represented as elastic rods. This setup allows DEFT to capture the geometric and physical properties required for dynamic simulation. To improve computational efficiency, DEFT then predicts the dynamics of each branch in parallel (Section IV-F). During this process, analytical gradients are provided to solve (10), as detailed in Section IV-C, ensuring efficient and stable convergence. Next, to address numerical errors, DEFT employs a GNN designed to learn the BDLO's residual dynamics (Section IV-D). By modeling discrepancies between simulated and observed behavior, the GNN refines predictions and enhances overall accuracy. After integration, DEFT enforces constraints (Section IV-E) to enforce physical realism. Inextensibility constraints are applied to each branch, while junction-level constraints ensure proper attachment at branch junctions. Additionally, edge orientation constraints enable the propagation of dynamics across these junctions. Throughout the entire pipeline, all components remain fully differentiable, allowing for efficient parameter learning from real-world data.

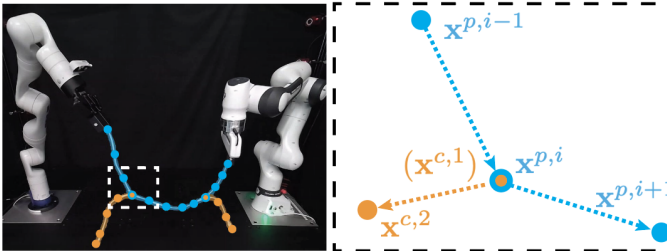


Fig. 4: An illustration of a branched deformable linear object (BDLO) model. Left: An example configuration of BDLO manipulation. Right: Relevant notation and structure at a junction.

simulation; and 4) a parallel programming strategy that ensures efficient simulation and gradient computation during training and simulation. Please note that to simplify the presentation, we omit the time subscript t in Sections IV-C and IV-E.

A. Branched Deformable Linear Object Model

To model a BDLO, we decompose its structure into a hierarchical arrangement of DLOs. The parent DLO is defined as the minimum-length path through the BDLO that connects the two end-effectors (i.e., the points where the structure is manipulated or anchored). All other branches diverging from this primary path are modeled as children DLOs that maintain their physical connection to the parent DLO at their attachment points, which we refer to as *junction points*. The parent and children DLOs are each modeled as DLOs and inherit all previously introduced notation. For conciseness, we describe the junction point using only three edges at each time instance: two from the parent DLO and one from a child DLO. In principle, the methods in DEFT can be extended to handle junctions with more than three edges.

We distinguish between the parent and child DLOs using superscripts p and c , respectively. For instance, if a junction is located at the i -th vertex, the associated edges are denoted by

$e_t^{p,i-1}$, $e_t^{p,i}$, and $e_t^{c,1}$. An illustration of a BDLO can be found in Figure 4. To capture the influence of bending and twisting, we introduce the moment of inertia of the i -th edge which is denoted by $\mathbf{I}^i \in \mathbb{R}^{3 \times 3}$. It represents how the segment's mass distribution affects its resistance to rotational deformations. The orientation of e_t^i is denoted by an angle axis vector $\Omega_t^i \in \mathbb{R}^3$.

Let the orientation and position of the two end effectors at time t be denoted by $\mathbf{u}_t \in \mathbb{R}^{12}$. We refer to \mathbf{u}_t as the input. We assume that the initial state of the BDLO is fully observable, and that it can be accurately estimated using image segmentation [31] in combination with Gaussian Mixture Models [32].

B. DEFT Overview

At each time t , DEFT simulates the behavior of a BDLO when given predictions of the vertices and their velocities under a specified input as described in Algorithm 1. It begins by first associating the grasped vertices with the robot end effector inputs \mathbf{u}_t . DEFT then processes the parent and children DLOs in parallel to compute their respective material frames using (3) (4), which are subsequently used to calculate each branch's potential energy. DEFT then minimizes this potential energy using analytical gradients to determine the optimal parameters θ_t^* and updates the potential energy accordingly (Line 2). These forces are integrated forward in time using a Semi-Implicit Euler method combined with residual learning to update the vertex velocities and positions (Lines 3 and 4).

However, due to numerical integration errors, branch lengths may change in length. In addition, up to this point, DEFT treats each branch's internal dynamics in isolation, without accounting for junction interactions. This omission can hinder the propagation of dynamics across junctions. For example, children DLOs may detach from their parent branches, or deformation effects (e.g., bending and twisting) may not propagate through the junction. To address these issues, DEFT

Algorithm 1 $(\hat{\mathbf{X}}_{t+1}, \hat{\mathbf{V}}_{t+1}) = \text{DEFT}(\hat{\mathbf{X}}_t, \hat{\mathbf{V}}_t, \mathbf{u}_t)$

- 1: Associate grasped vertices with \mathbf{u}_t
- 2: Calculate Material Frames $\Gamma(\mathbf{X}_t, \theta_t)$ \triangleright (3),(4)
- 3: $\theta_t^*(\mathbf{X}_t, \alpha) = \arg \min_{\theta_t} P(\Gamma(\mathbf{X}_t, \theta_t), \alpha)$ \triangleright Section.IV-C
- 4: $\hat{\mathbf{V}}_{t+1} = \hat{\mathbf{V}}_t - \Delta_t \mathbf{M}^{-1} \frac{\partial P(\Gamma(\mathbf{X}_t, \theta_t^*(\mathbf{X}_t, \alpha)), \alpha)}{\partial \mathbf{X}_t}$ \triangleright (7)
- 5: $\hat{\mathbf{X}}_{t+1} = \hat{\mathbf{X}}_t + \Delta_t \hat{\mathbf{V}}_{t+1} + \text{GNN}$ \triangleright Section.IV-D
- 6: Constraints enforcement on $\hat{\mathbf{X}}_{t+1}$ \triangleright Algorithm 2
- 7: $\hat{\mathbf{V}}_{t+1} = (\hat{\mathbf{X}}_{t+1} - \hat{\mathbf{X}}_t) / \Delta_t$ \triangleright Velocity Update

return $\hat{\mathbf{X}}_{t+1}, \hat{\mathbf{V}}_{t+1}$

enforces additional constraints to ensure each branch remains inextensible, maintain branch connections, and allow deformation effects to propagate across the junction (Line 5). By applying Algorithm 1 over multiple time increments, DEFT can accurately predict the BDLO's state over extended time horizons. An algorithm overview is illustrated in Figure 3.

C. Analytical Gradient Derivation

The goal of this subsection is to present the analytical gradient of $P(\Gamma(\mathbf{X}_t, \theta_t), \alpha)$ with respect to θ_t . To improve the paper's readability, we summarize the result in the following theorem whose proof can be found in Appendix A.

Theorem 1. *Let $\Gamma(\mathbf{X}_t, \theta_t)$ be the Material Frame at time t , and let α contain the bending stiffness $\mathbf{B} \in \mathbb{R}^{3 \times 3}$ and twisting stiffness $\beta \in \mathbb{R}$. Suppose the total potential energy is the sum of bending and twisting potential energies:*

$$P(\Gamma(\mathbf{X}_t, \theta_t), \alpha) = P_{\text{bend}}(\Gamma(\mathbf{X}_t, \theta_t), \mathbf{B}) + P_{\text{twist}}(\Gamma(\mathbf{X}_t, \theta_t), \beta). \quad (12)$$

Then the partial derivative of the bending and twisting potential energies with respect to θ^i are given by

$$\frac{\partial P_{\text{bend}}(\Gamma(\mathbf{X}_t, \theta_t), \alpha)}{\partial \theta^i} = \sum_{k=i}^{i+1} \left(\mathbf{B}^k (\omega^{(k,i)} - \bar{\omega}^{(k,i)}) \right)^T \begin{bmatrix} 0 & 1 \\ -1 & 0 \end{bmatrix} \omega^{(k,i)}, \quad (13)$$

$$\frac{\partial P_{\text{twist}}(\Gamma(\mathbf{X}_t, \theta_t), \alpha)}{\partial \theta^i} = \beta^i (\theta^i - \theta^{i-1}) - \beta^{i+1} (\theta^{i+1} - \theta^i), \quad (14)$$

respectively, where the material curvature $\omega^{(i,j)}$ is defined as

$$\omega^{(i,j)} = (\kappa \mathbf{b}^i \cdot \mathbf{m}_1^j, \kappa \mathbf{b}^i \cdot \mathbf{m}_2^j)^T \quad \text{for } j \in \{i-1, i\}, \quad (15)$$

$\bar{\omega}^{(i,j)}$ denotes the undeformed material curvature, and the curvature vector $\kappa \mathbf{b}^i$ in (15) is

$$\kappa \mathbf{b}^i = \frac{2 (\mathbf{e}^{i-1} \times \mathbf{e}^i)}{\|\mathbf{e}^{i-1}\|_2 \|\mathbf{e}^i\|_2 + \mathbf{e}^{i-1} \cdot \mathbf{e}^i}. \quad (16)$$

D. Integration Method with Residual Learning

This subsection constructs the GNN for residual learning in (11). The motivation for employing a GNN lies in its ability

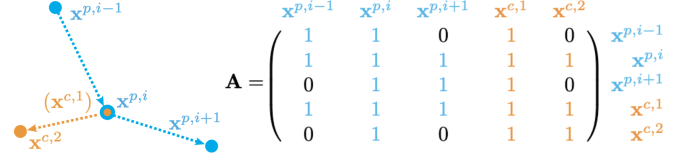


Fig. 5: The adjacency matrix \mathbf{A} for the junction in Figure 4 captures both self-loops (diagonal entries) and inter-node connections (off-diagonal entries). By embedding each node's local dynamics alongside its coupling to neighboring nodes, \mathbf{A} enables an graph representation of the BDLO's behavior.

to represent a BDLO as a graph, where each vertex is treated as a node and edges capture both intra-branch connections and junctions. This graph-based formulation translates into an adjacency matrix $\mathbf{A} \in \mathbb{R}^{(n^p+n^c) \times (n^p+n^c)}$, which links individual branch nodes and explicitly encodes node information across branch junctions. This adjacency matrix is defined as:

$$\mathbf{A}_{i_1, i_2} = \begin{cases} 1 & \text{if there is an edge between } i_1 \text{ and } i_2, \\ 0 & \text{otherwise,} \end{cases} \quad (17)$$

An illustration of \mathbf{A} can be found in Figure 5. In practice, DEFT constructs \mathbf{A} for each BDLO whose behavior a user wants to predict. This adjacency matrix is utilized within a Graph Convolutional Network (GCN) [33] to aggregate learned features. A single GCN layer is defined as

$$\text{GCN}(\hat{\mathbf{X}}_t, \hat{\mathbf{V}}_t, \alpha) = \tilde{\mathbf{A}} \mathbf{F}_t(\hat{\mathbf{X}}_t, \hat{\mathbf{V}}_t, \alpha) \mathbf{W}, \quad (18)$$

where $\tilde{\mathbf{A}}$ is the normalized adjacency matrix

$$\tilde{\mathbf{A}} = \mathbf{D}^{-\frac{1}{2}} \mathbf{A} \mathbf{D}^{-\frac{1}{2}}. \quad (19)$$

Note that $\tilde{\mathbf{A}}$ is the normalization of \mathbf{A} using the degree matrix $\mathbf{D} = \text{diag}(d_1, d_2, \dots, d_n)$ where $d_{i1} = \sum_{i2} A_{i1, i2}$. This normalization ensures that nodes with a high degree do not disproportionately influence the overall performance. This ensures consistent feature magnitudes across the learned representation [34]. The node feature matrix, $\mathbf{F}_t(\hat{\mathbf{X}}_t, \hat{\mathbf{V}}_t, \alpha) \in \mathbb{R}^{(n^p+n^c) \times h}$, is constructed by concatenating its arguments together. The trainable weight matrix $\mathbf{W} \in \mathbb{R}^{h \times 3}$ is implemented via a multi-layer perceptron (MLP) [35], which projects input features into latent representations.

E. Enforcing Constraints

After performing numerical integration, DEFT applies constraints to ensure branch inextensibility, ensure that branches are attached at the junctions, and ensure that deformations are propagated throughout the BDLO. To accomplish this, DEFT updates the positions of each vertex using correction terms $\Delta \hat{\mathbf{X}}$. One could just update the positions of each vertex by just projecting directly onto the constraint set. However, this induces highly nonlinear changes in momentum and can lead to simulation instability and unrealistic behavior.

Motivated by the PDB method [36], DEFT enforces the aforementioned constraints while trying to preserve momentum. DEFT does this by formulating the computation of the correction term as the solution to an optimization problem. As we illustrate through our experimental evaluation in Section

V , this leads to more stable simulations, which corresponds to more realistic predictions. Finally, note that DEFT could formulate the optimization problem to compute the correction terms as a single large optimization problem that considers constraints between all vertices in the BDLO simultaneously. However, this large optimization problem can be difficult to solve rapidly. Instead DEFT enforces these constraints sequentially between neighboring nodes. Next, we summarize each of these optimization problems.

1) *Inextensibility Enforcement*: To enforce inextensibility of each branch, we define a constraint function between successive vertices. This function penalizes deviations of each segment's length from its undeformed length. By applying the following theorem, whose proof can be found in [8, Appendix B.2], one can compute $\Delta\hat{\mathbf{x}}^i, \Delta\hat{\mathbf{x}}^{i+1}$ explicitly:

Theorem 2 (Computing the Corrections to Enforce Inextensibility). *Consider two successive vertices i and $i+1$ along the same branch. Let $\bar{\mathbf{e}}_i$ denote the edge between these vertices when the BDLO is undeformed. Let the constraint function to enforce inextensibility be defined as:*

$$C_I^i(\hat{\mathbf{X}}, \Delta\hat{\mathbf{X}}) = \|(\hat{\mathbf{x}}^i + \Delta\hat{\mathbf{x}}^i) - (\hat{\mathbf{x}}^{i+1} + \Delta\hat{\mathbf{x}}^{i+1})\|_2 - \|\bar{\mathbf{e}}_i\|_2. \quad (20)$$

The correction $\Delta\hat{\mathbf{X}}$ to enforce inextensibility at joint i can be computed by solving the following optimization problem:

$$\begin{aligned} \min_{\Delta\hat{\mathbf{X}}} \quad & \frac{1}{2} \left(C_I^i(\hat{\mathbf{X}}, \Delta\hat{\mathbf{X}}) \right)^2 \\ \text{s.t.} \quad & \Delta\hat{\mathbf{x}}^j = 0 \quad \forall j \notin \{i, i+1\}, \\ & \mathbf{M}^i \Delta\hat{\mathbf{x}}^i + \mathbf{M}^{i+1} \Delta\hat{\mathbf{x}}^{i+1} = \mathbf{0}, \\ & \mathbf{I}^i \hat{\Omega}_\Delta^i(\hat{\mathbf{X}}, \Delta\hat{\mathbf{X}}) = \mathbf{0}, \end{aligned} \quad (21)$$

where $\hat{\Omega}_\Delta^i(\hat{\mathbf{X}}, \Delta\hat{\mathbf{X}}) \in \mathbb{R}^3$ is defined in Appendix B and represents the orientation change of the i th edge arising from $\Delta\hat{\mathbf{x}}^i$ and $\Delta\hat{\mathbf{x}}^{i+1}$ and $\mathbf{0}$ correspond to the zero vector of appropriate size. The only non-zero elements of the minimizer to this optimization problem can be computed explicitly and are equal to:

$$\Delta\hat{\mathbf{x}}^i = \mathbf{M}^{i+1} (\mathbf{M}^i + \mathbf{M}^{i+1})^{-1} C_I^i(\hat{\mathbf{X}}, \mathbf{0}) \frac{(\hat{\mathbf{x}}^{i+1} - \hat{\mathbf{x}}^i)}{\|\hat{\mathbf{x}}^{i+1} - \hat{\mathbf{x}}^i\|_2}, \quad (22)$$

$$\Delta\hat{\mathbf{x}}^{i+1} = \mathbf{M}^i (\mathbf{M}^i + \mathbf{M}^{i+1})^{-1} C_I^i(\hat{\mathbf{X}}, \mathbf{0}) \frac{(\hat{\mathbf{x}}^i - \hat{\mathbf{x}}^{i+1})}{\|\hat{\mathbf{x}}^i - \hat{\mathbf{x}}^{i+1}\|_2}. \quad (23)$$

Note that the inextensibility constraint at vertex i is satisfied when $C_I^i(\hat{\mathbf{X}}, \mathbf{0})^2 = 0$. For convenience, let the function that computes the minimizer of optimization problem (21) using $\hat{\mathbf{X}}$ be denoted by D_I^i (i.e., $D_I^i : \hat{\mathbf{X}} \mapsto \Delta\hat{\mathbf{X}}$).

2) *Enforcing Attachment at the Junction*: To ensure the child branch remains attached to the parent branch, we define a constraint function between their junction vertices. By applying the following theorem, whose proof can be found in Appendix C, one can compute $\Delta\hat{\mathbf{x}}^{p,i}, \Delta\hat{\mathbf{x}}^{c,1}$ explicitly:

Theorem 3. *Consider the parent-branch vertex $\hat{\mathbf{x}}^{p,i}$ and child-branch vertex $\hat{\mathbf{x}}^{c,1}$ at the junction such as the one depicted in Figure 4. Let the constraint function to enforce attachment at*

the junction be defined as:

$$C_A^{p,i}(\hat{\mathbf{X}}, \Delta\hat{\mathbf{X}}) = \|(\hat{\mathbf{x}}^{p,i} + \Delta\hat{\mathbf{x}}^{p,i}) - (\hat{\mathbf{x}}^{c,1} + \Delta\hat{\mathbf{x}}^{c,1})\|_2. \quad (24)$$

Suppose that the correction $\Delta\hat{\mathbf{X}}$ to account for the junction attachment constraint is obtained by solving an optimization problem that is identical to (21) with the objective function replaced with (24) and with a requirement that the only elements of $\Delta\hat{\mathbf{X}}$ are those associated vertices p, i and $c, 1$. The only non-zero elements of the minimizer to this optimization problem can be computed explicitly and are equal to:

$$\begin{aligned} \Delta\hat{\mathbf{x}}^{p,i} &= \mathbf{M}^{c,1} (\mathbf{M}^{p,i} + \mathbf{M}^{c,1})^{-1} C_A^{p,i}(\hat{\mathbf{X}}, \mathbf{0}) \frac{(\hat{\mathbf{x}}^{c,1} - \hat{\mathbf{x}}^{p,i})}{\|\hat{\mathbf{x}}^{c,1} - \hat{\mathbf{x}}^{p,i}\|_2}, \\ \Delta\hat{\mathbf{x}}^{c,1} &= \mathbf{M}^{p,i} (\mathbf{M}^{p,i} + \mathbf{M}^{c,1})^{-1} C_A^{p,i}(\hat{\mathbf{X}}, \mathbf{0}) \frac{(\hat{\mathbf{x}}^{p,i} - \hat{\mathbf{x}}^{c,1})}{\|\hat{\mathbf{x}}^{p,i} - \hat{\mathbf{x}}^{c,1}\|_2}. \end{aligned}$$

Note that the junction attachment constraint is satisfied at vertex p, i when $C_A^{p,i}(\hat{\mathbf{X}}, \mathbf{0})^2 = 0$. For convenience, let the function that computes the minimizer of optimization problem (21) using $\hat{\mathbf{X}}$ be denoted by $D_A^{p,i}$ (i.e., $D_A^{p,i} : \hat{\mathbf{X}} \mapsto \Delta\hat{\mathbf{X}}$).

3) *Edge Orientation Constraints at the Junction*: Many practical wire-harnesses feature junctions that are nearly rigid. This near-rigidity arises because manufacturers often use rigid plastics or other stiff materials at these connection points [37]. This results in minimal rotational or bending freedom. Consequently, the dynamics between the parent and child branches propagate through the junction in an almost rigid manner. To capture this behavior, we model each edge as a rigid body and define a constraint function that computes the relative orientation of each body. We then require that this constraint function is approximately satisfied where $\Delta\hat{\mathbf{x}}^{p,i}, \Delta\hat{\mathbf{x}}^{c,1}$ are computed. By applying the following theorem, whose proof can be found in Appendix D, one can compute $\Delta\hat{\mathbf{x}}^{p,i}, \Delta\hat{\mathbf{x}}^{c,1}$ explicitly:

Theorem 4. *Consider the parent-branch vertex $\hat{\mathbf{x}}^{p,i}$ and child-branch vertex $\hat{\mathbf{x}}^{c,1}$ at the junction such as the one depicted in Figure 4. Let $\epsilon > 0$ be a user specified parameter. Let the constraint function to enforce the orientation of the junction be defined as:*

$$C_O^{p,i}(\hat{\mathbf{X}}, \Delta\hat{\mathbf{X}}) = \|(\hat{\Omega}^{p,i}(\hat{\mathbf{X}}, \Delta\hat{\mathbf{X}}) + \hat{\Omega}_\Delta^{p,i}(\hat{\mathbf{X}}, \Delta\hat{\mathbf{X}})) - (\hat{\Omega}^{c,i}(\hat{\mathbf{X}}, \Delta\hat{\mathbf{X}}) + \hat{\Omega}_\Delta^{c,i}(\hat{\mathbf{X}}, \Delta\hat{\mathbf{X}})\|_2 - \epsilon, \quad (25)$$

where $\hat{\Omega}_\Delta$ and $\hat{\Omega}$ are defined in Appendix B and $\epsilon > 0$ bounds the mismatch between the updated parent-child orientation and the original orientation, ensuring that each junction remains almost rigid. The orientation correction at the junction is obtained by solving the following optimization problem:

$$\begin{aligned} \min_{\Delta\hat{\mathbf{X}}} \quad & \frac{1}{2} \left(C_O^{p,i}(\hat{\mathbf{X}}, \Delta\hat{\mathbf{X}}) \right)^2 \\ \text{s.t.} \quad & \mathbf{I}^{p,i} \hat{\Omega}_\Delta^{p,i} + \mathbf{I}^{c,1} \hat{\Omega}_\Delta^{c,i} = \mathbf{0} \end{aligned} \quad (26)$$

When Δ_t is sufficiently small, then one can compute explicit formulas for $\Delta\hat{\mathbf{X}}$ which can be found in Appendix D.

Note that the junction orientation constraint is satisfied at vertex p, i when $C_O^{p,i}(\hat{\mathbf{X}}, \mathbf{0})^2 = 0$. For convenience, let the

Algorithm 2 Momentum Preserving Constraint Enforcement

Require: $X_{t+1}, \kappa > 0$

```

1: while  $\exists(i, j)$  such that  $C_j^i(\hat{\mathbf{X}}_{t+1}, \mathbf{0})^2 > \kappa$  do
2:   for  $i = 1$  to  $n - 1$  do
3:      $\hat{\mathbf{X}}_{t+1} = \hat{\mathbf{X}}_{t+1} + D_I^i(\hat{\mathbf{X}}_{t+1})$             $\triangleright$  Theorem 2
4:     if  $i$ th segments is a junction then
5:        $\hat{\mathbf{X}}_{t+1} = \hat{\mathbf{X}}_{t+1} + D_A^i(\hat{\mathbf{X}}_{t+1})$             $\triangleright$  Theorem 3
6:        $\hat{\mathbf{X}}_{t+1} = \hat{\mathbf{X}}_{t+1} + D_O^i(\hat{\mathbf{X}}_{t+1})$             $\triangleright$  Theorem 4
7:     end if
8:   end for
9: end while
10: return :  $\hat{\mathbf{X}}_t$                                       $\triangleright$  Updated Vertices

```

function that computes the minimizer of optimization problem (21) using $\hat{\mathbf{X}}$ be denoted by $D_O^{p,i}$ (i.e., $D_O^{p,i} : \hat{\mathbf{X}} \mapsto \Delta\hat{\mathbf{X}}$).

4) Algorithm to Implement Corrections Due To Constraint Enforcement: As described earlier, we run each of these optimization problems sequentially to generate a correction to the output of the integration method (Line 5 in Algorithm 1). This is summarized in Algorithm 2. Note that one begins by checking whether any constraint is violated by more than some user-specified parameter κ . If any of the constraints are violated by more than κ , then one applies the correction described in the previous subsections to modify the prediction. This repeats until all constraints are satisfied.

F. Parallel Programming

We implement DEFT using PyTorch [26], taking advantage of its batch operations to execute Algorithm 1. PyTorch’s support for batch-wise computations enables parallel processing of multiple parent and child branch instances, significantly enhancing computational efficiency as we illustrate empirically in Section V-D. Specifically, the first batch is dedicated to executing the parent branch’s algorithm, while the remaining batches handle executions for the children branches.

One challenge arises when the number of nodes in the parent branch (n^p) differs from the number in a child branch (n^c). This dimensional mismatch prevents the direct construction of uniform matrices for batch operations. To overcome this, we assume $n^p > n^c$ and introduce padded matrices and vertices by appending zeros to the child branch's structure to match the parent branch's dimensions. This strategy ensures uniform matrix construction across the batches, which facilitates seamless batch-wise operations. During parameter updates, we mask out the gradients from padded elements to prevent them from influencing the learned parameters.

V. EXPERIMENTS AND RESULTS

This section presents the real-world evaluation of DEFT, covering: 1) A quantitative accuracy comparison with state-of-the-art methods, including scenarios where grasping occurs at various points along the BDLO, such as parent-branch ends and midpoints; 2) An assessment of DEFT's inference speed; 3) An ablation study exploring parameter auto-tuning, residual

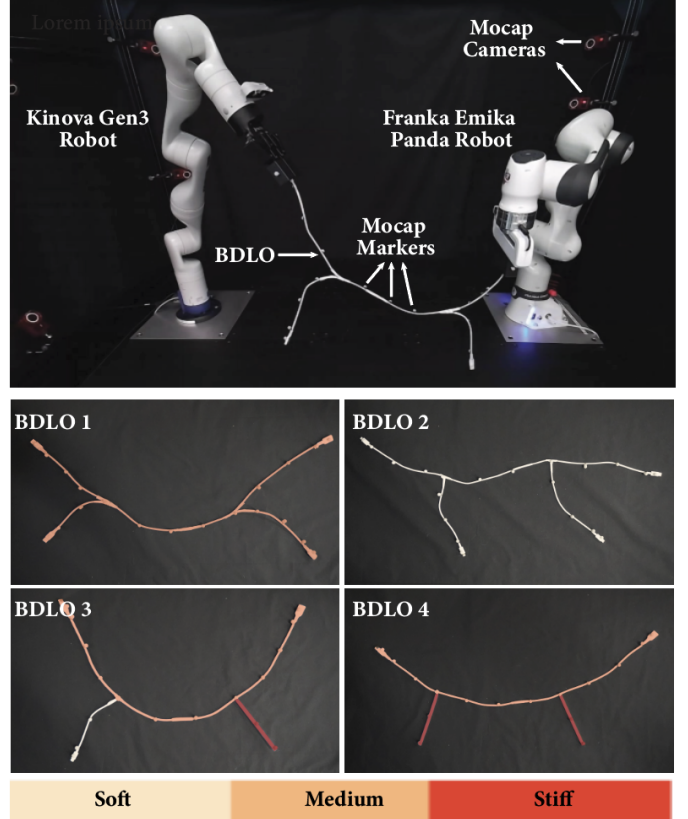


Fig. 6: An illustration of experiment setup. Top: Data collection setup with a dual-arm robot. Bottom: An illustration of the BDLOs used to evaluate and compare the performance of DEFT against baseline methods. To increase dataset diversity, we vary the BDLOs' stiffness, length, weights, number of vertices, and junction structures.

learning, and a naive multi-branch approach that connects multiple single-DLO models; 4) Shape-matching manipulation demonstrations, highlighting DEFT’s real-world manipulation efficacy; 5) Thread insertion manipulation demonstrations, showcasing DEFT’s versatility. Code and data will be made publicly available upon final paper acceptance. To the best of our knowledge, this will be the first publicly available dataset and code for modeling BDLOs.

A. Hardware Setup

1) Hardware Setup: Four distinct BDLOs were constructed to validate DEFT's modeling accuracy as shown at the bottom of Figure 6. The material stiffness description of each BDLO is outlined in Table I. Note that we introduced stiff child branches attached to the parent branch in BDLO3 and BDLO4. These branches represent the rigid components (e.g., fixations) commonly used in BDLO construction [37]. These attachments help ensure secure mounting, preserve structural integrity, and manage loads in real-world applications. Spherical markers were attached to each BDLO to facilitate dataset creation for both training and evaluation, with the number of vertices set equal to the number of MoCap markers. Because the markers are present during both training and evaluation, their

TABLE I: A summary of each BDLO’s material properties and marker count used in the real-world experiment. Stiffness is estimated based on a relative scale.

BDLO	Parent Stiffness / #Markers	Child1 Stiffness / #Markers	Child2 Stiffness / #Markers	Dataset 1 Time (s)	Dataset 2 Time (s)
1	Medium / 13	Medium / 4	Medium / 3	505	440
2	Low / 12	Low / 4	Low / 4	735	N/A
3	Medium / 12	Low / 2	High / 3	645	445
4	Medium / 12	High / 2	High / 2	495	N/A

impact on the BDLO dynamics is inherently accounted within all subsequent analyses. If one wishes to obtain a BDLO dataset without relying on real-world motion capture, a finite element method-based simulator could be employed. Note that the markers are *only* used to create training and evaluation datasets, as well as evaluate the performance of DEFT by providing the ground truth. However, for real-world applications, the markers are not needed. For dual manipulation, a Franka Emika Research 3 robot and a Kinova Gen3 robot were used. An illustration of the experimental setup is shown in Figure 6. We used an OptiTrack motion capture system to record ground-truth vertex locations. Note in our implementation of DEFT we set $\epsilon = 0.1$ (Theorem 4) and $\kappa = 0.02$ (Algorithm 2).

2) *Dataset Collection and Training*: We collected dynamic trajectory data for selected BDLOs in the real world using a motion capture system operating at 100 Hz, capturing both slow and fast BDLO motions, as illustrated at the top of Figure 6. We split our data collection into two categories:

- Dataset 1: each robot grasps one end of the BDLO. Data from this category were collected for all BDLOs.
- Dataset 2: One robot grasped one end of the BDLO while the other robot grasped the BDLO at its midpoint. This dataset is collected for BDLOs 1 and 3.

Total collection times are provided in Table I. The dataset is split with $\sim 75\%$ for training and $\sim 25\%$ for evaluation. The model for each of the four BDLOs is trained separately using the trajectory data collected from our real-world experiments. During training, models are trained using the same 100 steps (i.e., 1s) of dynamic motion. Each method’s performance is evaluated when predicting the state of the wire over a 500 step (i.e. 5s) prediction horizon using just the state of the wire at the initial time and the orientation and position of the two end effectors at each time step.

B. Baseline Comparisons

Only a limited number of papers have investigated the dynamic behavior of BDLOs, and none provide a differentiable framework for learning real-world dynamics from real-world datasets. Moreover, no public code repositories are available for these approaches, making direct replication infeasible. We select two available implementations, Tree-LSTM [38] and GCN [33] as baseline prediction models for BDLOs. Tree-LSTM and GCN both capture structured relationships. Specifically, Tree-LSTM leverages hierarchical tree representations,

TABLE II: Modeling Results Over a 5s Horizon

Method	Modeling Accuracy (RMSE, 10^{-2} m)					
	Dataset 1				Dataset 2	
	1	2	3	4	1	3
GCN [33]	6.70	6.42	5.25	4.20	7.33	4.24
Tree-LSTM [38]	5.32	4.50	2.46	2.71	7.08	4.55
DEFT	1.87	2.82	1.51	1.41	1.49	1.80

TABLE III: One Step Inference Time with Dataset 1

Method	Time (10^{-2} s)			
	1	2	3	4
GCN [33]	0.20	0.19	0.13	0.13
Tree-LSTM [38]	1.81	2.44	1.79	1.89
DEFT	0.76	0.70	0.91	0.93

while GCN excels in graph-based modeling. Because BDLOs can be described by nodes and edges, these architectures are naturally able to incorporate a BDLO’s dynamics.

C. Modeling Results

Table II summarizes the average RMSE loss when comparing DEFT to baseline methods for two categories of dataset. Performance is evaluated over a 5 second prediction horizon for four different BDLOs. Note that DEFT outperforms all baselines across all four BDLOs. An illustration of the performance of DEFT, Tree-LSTM, and an ablation of DEFT, which is described in more detail in the next subsection, can be found in Figure 7. A video of related experiments can be found in the supplementary material.

D. Computational Experiment

This section evaluates the computational efficiency of DEFT when compared to baseline methods. It also examines how employing the analytical gradient derived from Theorem 1 to compute (10) and the parallel programming approach detailed in Section IV-F, impacts overall computational time. All experiments in this section were conducted in Python on an Ubuntu 20.04 equipped with an AMD Ryzen PRO 5995WX CPU, 256GB of RAM, and 128 cores.

1) *Computational Speed Comparison*: We compare computational speed for one step inference. Table III indicates that GCN has the fastest speed. DEFT is the second fastest and is able to generate single step predictions at a 100Hz frequency.

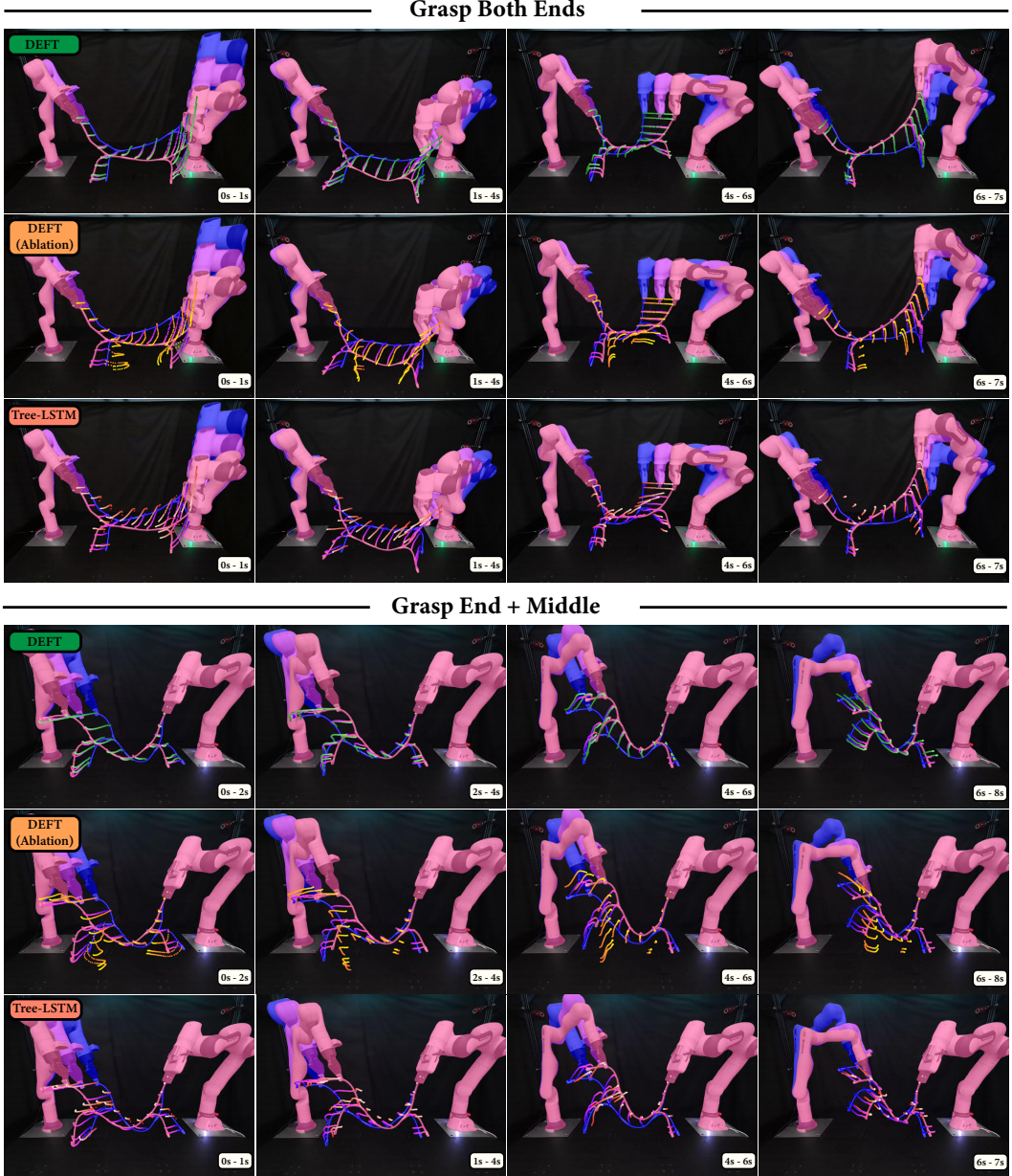


Fig. 7: Visualization of the predicted trajectories for BDLO 1 under two manipulation scenarios, using DEFT, a DEFT ablation that leaves out the constraint described in Theorem 4, and Tree-LSTM. The ground-truth initial position of the vertices are colored in blue, the ground-truth final position of the vertices are colored in pink, and the gradient between these two colors is used to denote the ground truth location over time. The predicted vertices are colored as green circles (DEFT), orange circles (DEFT ablation), and light red circles (Tree-LSTM), respectively. A gradient is used for these predictions to depict the evolution of time, starting from dark and going to light. Note that the ground truth is only provided at $t=0$ s and prediction is constructed until $t=8$ s. The prediction is performed recursively, without requiring additional ground-truth data or perception inputs throughout the entire process.

2) *Computational Speed with Analytical Gradient*: We compare the computational speed of using analytical gradients when compared to using numerical gradients. As summarized in Table IV, computing (10) with the analytical gradient is approximately twice as fast as using numerical gradients.

3) *Computational Speed with Parallel Programming*: We compare the computational performance of using parallel programming approach described in Section IV-F to a naive (sequential) implementation, in which each branch is simulated one after the other. In this experiment, we use the material

TABLE IV: Computational Time for (10) with Dataset 1

Method	Time (10^{-2} s)			
	1	2	3	4
Analytical Gradient	0.34	0.27	0.41	0.46
Numerical Gradient	0.74	0.65	0.84	0.91

properties of BDLO1 and gradually increase the number of children branches from 1 to 8. As shown in Figure 9, the

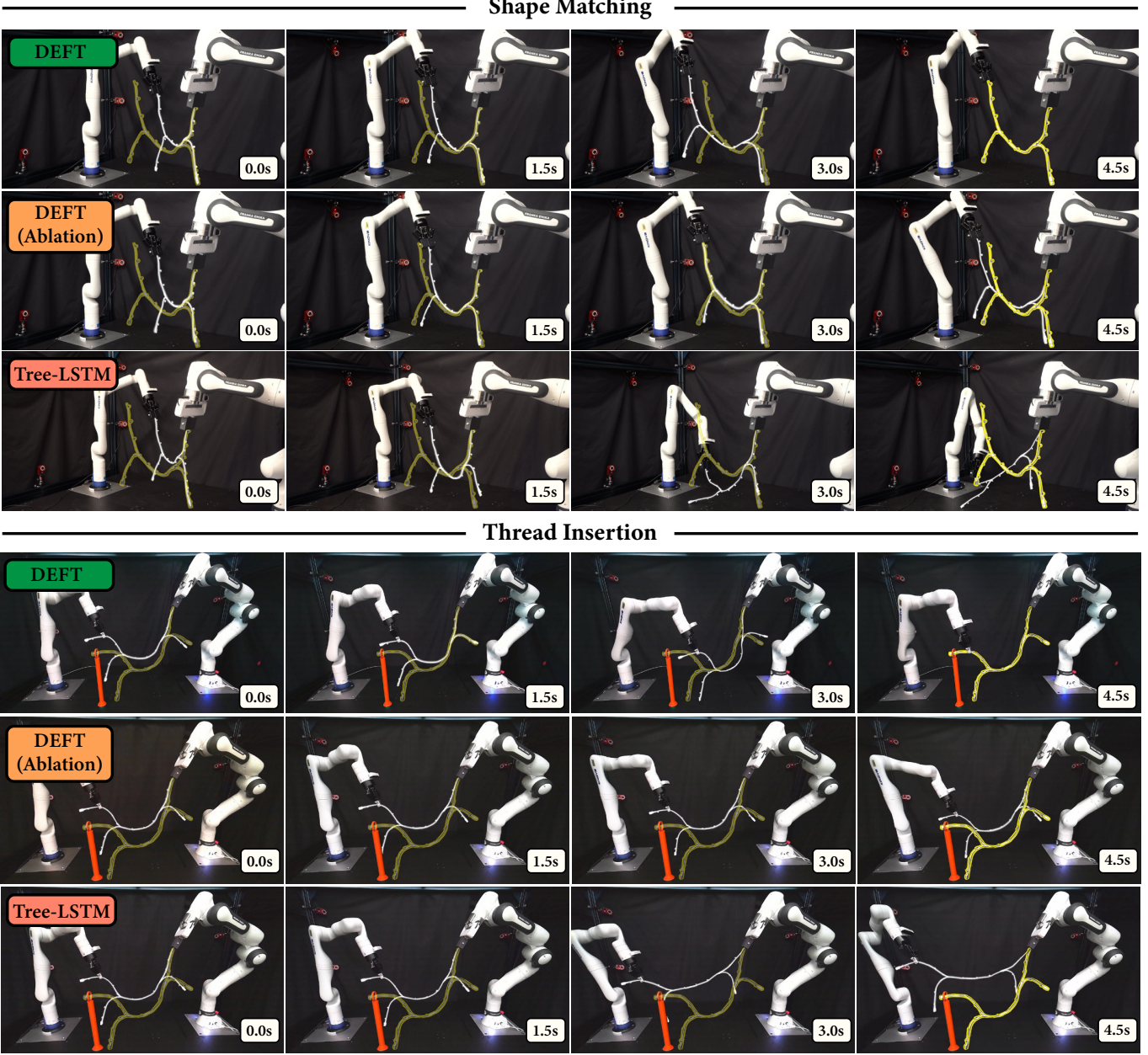


Fig. 8: Visualization of planning for BDLO 1 for two manipulation tasks, using DEFT, a DEFT ablation that leaves out the constraint described in Theorem 4, and Tree-LSTM. The BDLO’s goal configuration is highlighted in yellow, while the target hole is shown in red. The DEFT model enables the planning algorithm to successfully complete the task, whereas the ablation approach of DEFT and the Tree-LSTM model both fail to finish tasks.

naive implementation’s computation time grows more rapidly than that of the parallel approach. However, a certain increase in computational time is still expected with parallelization. As illustrated in Figure 3, constraints at each junction between the parent branch and its child branches prevent a fully batch-based operation, thereby resulting in an increase in the computational time.

E. Ablation Study

The results presented in Table V demonstrate the contribution of each DEFT component. Notably, excluding Theorems

2, 3, and 4 causes a significant increase in prediction loss. This outcome is primarily driven by the absence of Theorem 2, which leads to simulation instability. Although residual learning is used to mitigate errors, directly modeling stiff behaviors, such as the inextensibility of DLOs, remains challenging, making the learning process highly sensitive to inputs and hampering effective gradient propagation. A key challenge in using neural networks to learn position-based constraints is that constraints such as inextensibility confine the system to a low-dimensional manifold within a high-dimensional space. Without these constraints, it becomes difficult for the network

TABLE V: Ablation Study with Dataset 1

Method	Modeling Accuracy (RSME, 10^{-2} m) \downarrow					
	Dataset 1				Dataset 2	
	1	2	3	4	1	2
W/O Constraints.2, 3 and 4	7.66×10^8	6.10×10^8	6.56×10^6	1.77×10^8	3.81×10^7	1.23×10^8
W/O Constraints.3 and 4	1.36×10^2	1.81×10^2	1.51×10^2	7.64×10^1	8.72×10^1	3.38×10^2
W/O Constraint.4	3.95	3.49	2.03	2.15	4.01	4.88
W/O Learning + System ID	2.46	3.53	1.85	1.77	2.03	2.21
W/O System ID	2.24	3.00	1.67	1.50	1.66	1.95
W/O Residual Learning	1.93	3.19	1.70	1.62	1.86	1.89
Full Model	1.87	2.82	1.51	1.41	1.49	1.80

TABLE VI: Real-World Trajectory Planning Results

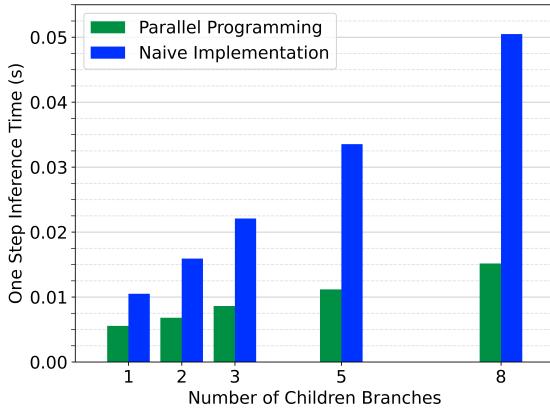


Fig. 9: Computational speed comparison: parallel programming versus a naive (sequential) implementation.

alone to keep the system on that manifold. Over multiple open-loop predictions, even minor errors can accumulate and push the system state off the manifold, causing reduce of residual learning’s effect. Similarly, removing Theorem 3 allows the children branch to detach from parent branch, and therefore fall freely under gravity, leading to a substantial increase in loss. Moreover, excluding Theorem 4 reduces accuracy, demonstrating the importance of introducing rigidity at junctions to allow dynamic propagation across branches.

Despite these challenges, auto-tuning the material properties provides the most substantial improvement over the baseline, illustrating DEFT’s ability to leverage real-world data for parameter identification. Residual learning also yields a non-trivial performance gain. By contrast, the model that do not learn from real-world data underperforms those that do, illustrating the importance of differentiability in this framework.

F. Planning Results

This section demonstrates how these BDLO models can be used for planning tasks, including shape matching and thread insertion. We compare three approaches: DEFT, which is our proposed method; DEFT without the constraint described in Theorem 4, an ablation approach that removes rigidity at junctions and thus limits dynamic propagation across branches;

	Successful Rate	
	Shape Matching	Thread Insertion
Tree-LSTM [38]	2/40	0/35
DEFT w/o Theorem 4	27/40	16/35
DEFT	35/40	29/35

Tree-LSTM, the baseline model with performance closest to DEFT. In these experiments, we employ ARMOUR [39], a receding-horizon trajectory planner and tracking controller, to manipulate BDLOs. ARMOUR relies on each model’s predicted BDLO states to guide the BDLO to a desired final configuration. Further details on integrating ARMOUR with BDLO simulators are provided in Appendix E. The results are summarized in Table VI, and Figure 8 shows one of the real-world results. A video of these experiments can be found in the supplementary material.

1) *Shape Matching*: In this experiment a goal configuration for the wire is specified and a random initial condition for the wire is chosen. A trial is considered successful if the Euclidean distance between each ground-truth vertex and its corresponding target vertex after planning is less than 0.05 m. If the task is not completed within 30 seconds, the trial is marked as a failure. As summarized in Table VI (left column), DEFT achieves a higher success rate than the other two models. Note that these experiments were all conducted in the real-world which further demonstrates the practical applicability of DEFT.

2) *Thread Insertion*: In this experiment, the planning algorithm must insert the end of the BDLO into a hole of radius 2.5cm which is placed in arbitrary location. The process consists of two stages—shape matching and thread insertion—which together require two goal configurations for the wire. Unlike the previous experiment, in which the robot grasps the branch end, the robot’s end effector clamps the third vertex from the branch’s insertion point. The trial is deemed successful if the BDLO branch successfully passes through the torus while also matching the user-specified wire shape successfully. As shown in Table VI (right column), DEFT again achieves a higher success rate than the other two models. Note that these experiments were all conducted in the real-

world which further demonstrates the practical applicability of DEFT.

VI. LIMITATIONS

While DEFT shows promising results in modeling and control of BDLOs, several limitations remain that could be addressed in future work. First, DEFT currently lacks a contact model for accurately predicting interactions between deformable components and their surroundings. Incorporating a contact modeling framework, such as that proposed in [40], would enable more realistic simulations and more robust planning in environments where collisions and frictional forces play a significant role. Second, for the insertion tasks considered in this work, we assume that the location and geometry of the target hole are known in advance. In unstructured or partially observed environments, this assumption may not hold. Incorporating 3D scene understanding methods, such as Gaussian Splatting [41], could help autonomously detect or refine the location of target features and thereby increasing the system’s applicability to real-world scenarios. Lastly, this work does not account for the orientation of the gripper during BDLO manipulation, which can significantly affect deformation behavior. As discussed in [16], gripper orientation can influence the kinematics of deformable objects. Future extensions of DEFT should therefore incorporate a more comprehensive treatment of gripper orientation to improve accuracy and expand the range of manipulable tasks.

VII. CONCLUSION

This paper introduces DEFT, a method that embeds residual learning within a novel differentiable branched Deformable Linear Object (BDLO) simulator. DEFT enables accurate modeling and real-time prediction of a BDLO’s dynamic behavior over long time horizons under dynamic manipulation. To demonstrate DEFT’s efficacy, we conduct a comprehensive set of experiments evaluating its accuracy, computational speed, impacts of its contribution and utility for manipulation tasks. Compared to the state of the art, DEFT achieves higher accuracy while remaining sample-efficient and without compromising computational speed. This paper also illustrates how to integrate DEFT with a planning and control framework for 3D shape matching and thread insertion of a BDLO in real-world scenarios. DEFT successfully completes more complex, real-world manipulation tasks than other tested baselines.

ACKNOWLEDGEMENT

The authors would like to gratefully thank the support by Ford Motor Company.

REFERENCES

[1] Jose Sanchez, Juan-Antonio Corrales, Belhassen-Chedli Bouzgarrou, and Youcef Mezouar. Robotic manipulation and sensing of deformable objects in domestic and industrial applications: a survey. *The International Journal of Robotics Research*, 37(7):688–716, 2018.

[2] Hao Wang, Omkar Salunkhe, Walter Quadrini, Dan Lämkull, Fredrik Ore, Björn Johansson, and Johan Stahre. Overview of computer vision techniques in robotized wire harness assembly: Current state and future opportunities. *Procedia CIRP*, 120:1071–1076, 2023. 56th CIRP International Conference on Manufacturing Systems 2023.

[3] Mitul Saha and Pekka Isto. Manipulation planning for deformable linear objects. *IEEE Transactions on Robotics*, 23(6):1141–1150, 2007.

[4] Miklós Bergou, Max Wardetzky, Stephen Robinson, Basile Audoly, and Eitan Grinspun. Discrete elastic rods. In *ACM SIGGRAPH 2008 Papers*, SIGGRAPH ’08, New York, NY, USA, 2008. Association for Computing Machinery.

[5] Naijing Lv, Jianhua Liu, Xiaoyu Ding, and Haili Lin. Assembly simulation of multi-branch cables. *Journal of Manufacturing Systems*, 45:201–211, 2017.

[6] A. Theeten and L. Grisoni. A robust and efficient lagrangian constraint toolkit for the simulation of 1d structures. *Computer-Aided Design*, 41(12):990–998, 2009.

[7] B. Nadler and M. B. Rubin. Post-buckling behavior of nonlinear elastic beams and three-dimensional frames using the theory of a cosserat point. *Mathematics and Mechanics of Solids*, 9(4):369–398, 2004.

[8] Yizhou Chen, Yiting Zhang, Zachary Brei, Tiancheng Zhang, Yuzhen Chen, Julie Wu, and Ram Vasudevan. Differentiable discrete elastic rods for real-time modeling of deformable linear objects. *arXiv preprint arXiv:2406.05931*, 2024.

[9] Fei Liu, Entong Su, Jingpei Lu, Mingen Li, and Michael C. Yip. Differentiable robotic manipulation of deformable rope-like objects using compliant position-based dynamics, 2022.

[10] Mengyao Ruan, Dale McConachie, and Dmitry Berenson. Accounting for directional rigidity and constraints in control for manipulation of deformable objects without physical simulation. In *2018 IEEE/RSJ International Conference on Intelligent Robots and Systems (IROS)*, pages 512–519, 2018.

[11] Mengyuan Yan, Yilin Zhu, Ning Jin, and Jeannette Bohg. Self-supervised learning of state estimation for manipulating deformable linear objects, 2020.

[12] Changhao Wang, Yuyou Zhang, Xiang Zhang, Zheng Wu, Xing-hao Zhu, Shiyu Jin, Te Tang, and Masayoshi Tomizuka. Offline-online learning of deformation model for cable manipulation with graph neural networks. *IEEE Robotics and Automation Letters*, 7(2):5544–5551, April 2022.

[13] David Baraff and Andrew Witkin. Large steps in cloth simulation. In *Proceedings of the 25th Annual Conference on Computer Graphics and Interactive Techniques*, SIGGRAPH ’98, page 43–54, New York, NY, USA, 1998. Association for Computing Machinery.

[14] Junbang Liang, Ming Lin, and Vladlen Koltun. Differentiable cloth simulation for inverse problems. In H. Wallach, H. Larochelle, A. Beygelzimer, F. d’Alché-Buc, E. Fox, and R. Garnett, editors, *Advances in Neural Information Processing Systems*, volume 32. Curran Associates, Inc., 2019.

[15] Tiantian Liu, Adam W. Bargteil, James F. O’Brien, and Ladislav Kavan. Fast simulation of mass-spring systems. *ACM Transactions on Graphics*, 32(6):209:1–7, November 2013. Proceedings of ACM SIGGRAPH Asia 2013, Hong Kong.

[16] Dmitry Berenson. Manipulation of deformable objects without modeling and simulating deformation. In *2013 IEEE/RSJ International Conference on Intelligent Robots and Systems*, pages 4525–4532, 2013.

[17] Marcos García, César Mendoza, Luis Pastor, and Angel Rodríguez. Optimized linear fem for modeling deformable objects. *Computer Animation and Virtual Worlds*, 17(3-4):393–402, 2006.

[18] Fun Shing Sin, Daniel Schroeder, and Jernej Barbič. Vega: nonlinear fem deformable object simulator. In *Computer Graphics Forum*, volume 32, pages 36–48. Wiley Online Library, 2013.

[19] Adrien Koessler, N Roca Filella, Belhassen-Chedli Bouzgarrou,

Laurent Lequievre, and J-A Corrales Ramon. An efficient approach to closed-loop shape control of deformable objects using finite element models. In *2021 IEEE International Conference on Robotics and Automation (ICRA)*, pages 1637–1643. IEEE, 2021.

[20] Avishai Sintov, Steve Macenski, Andy Borum, and Timothy Bretl. Motion planning for dual-arm manipulation of elastic rods. *IEEE Robotics and Automation Letters*, PP:1–1, 07 2020.

[21] Timothy Bretl and Zoe McCarthy. Quasi-static manipulation of a kirchhoff elastic rod based on a geometric analysis of equilibrium configurations. *The International Journal of Robotics Research*, 33:48 – 68, 2014.

[22] Dezhong Tong, Andrew Choi, Longhui Qin, Weicheng Huang, Jungseock Joo, and M. Khalid Jawed. Sim2real neural controllers for physics-based robotic deployment of deformable linear objects, 2023.

[23] Yili Zhao and Jernej Barbič. Interactive authoring of simulation-ready plants. *ACM Trans. Graph.*, 32(4), July 2013.

[24] Richard Bishop. There is more than one way to frame a curve. *The American Mathematical Monthly*, 82:Mathematical Association of America-, 03 1975.

[25] Luis Pineda, Taosha Fan, Maurizio Monge, Shobha Venkataraman, Paloma Sodhi, Ricky T. Q. Chen, Joseph Ortiz, Daniel DeTone, Austin Wang, Stuart Anderson, Jing Dong, Brandon Amos, and Mustafa Mukadam. Theseus: A library for differentiable nonlinear optimization, 2023.

[26] Adam Paszke, Sam Gross, Francisco Massa, Adam Lerer, James Bradbury, Gregory Chanan, Trevor Killeen, Zeming Lin, Natalia Gimelshein, Luca Antiga, Alban Desmaison, Andreas Köpf, Edward Yang, Zach DeVito, Martin Raison, Alykhan Tejani, Sasank Chilamkurthy, Benoit Steiner, Lu Fang, Junjie Bai, and Soumith Chintala. Pytorch: An imperative style, high-performance deep learning library, 2019.

[27] Kaiming He, Xiangyu Zhang, Shaoqing Ren, and Jian Sun. Deep residual learning for image recognition, 2015.

[28] Cheng Chi, Benjamin Burchfiel, Eric Cousineau, Siyuan Feng, and Shuran Song. Iterative residual policy for goal-conditioned dynamic manipulation of deformable objects. In *Proceedings of Robotics: Science and Systems (RSS)*, 2022.

[29] Yuxuan Yang, Johannes Stork, and Todor Stoyanov. Learning to propagate interaction effects for modeling deformable linear objects dynamics. pages 1950–1957, 05 2021.

[30] Yu She, Shaoxiong Wang, Siyuan Dong, Neha Sunil, Alberto Rodriguez, and Edward Adelson. Cable manipulation with a tactile-reactive gripper, 2020.

[31] Alexander Kirillov, Eric Mintun, Nikhila Ravi, Hanzi Mao, Chloe Rolland, Laura Gustafson, Tete Xiao, Spencer Whitehead, Alexander C. Berg, Wan-Yen Lo, Piotr Dollár, and Ross Girshick. Segment anything, 2023.

[32] Markus Wnuk, Chistoph Hinze, Manuel Zürn, Qizhen Pan, Armin Lechler, and Alexander Verl. Tracking branched deformable linear objects with structure preserved registration by branch-wise probability modification. In *2021 27th International Conference on Mechatronics and Machine Vision in Practice (M2VIP)*, pages 101–108, 2021.

[33] Thomas N. Kipf and Max Welling. Semi-supervised classification with graph convolutional networks, 2017.

[34] Jie Zhou, Ganqu Cui, Shengding Hu, Zhengyan Zhang, Cheng Yang, Zhiyuan Liu, Lifeng Wang, Changcheng Li, and Maosong Sun. Graph neural networks: A review of methods and applications, 2021.

[35] Walter H. Delashmit, Lockheed Martin Missiles, and Michael T. Manry. Recent developments in multilayer perceptron neural networks. 2005.

[36] Matthias Müller, Bruno Heidelberger, Marcus Hennix, and John Ratcliff. Position based dynamics. *J. Vis. Comun. Image Represent.*, 18(2):109–118, apr 2007.

[37] Jerome Trommnau, Jens Kühnle, Jörg Siegert, Robert Inderka, and Thomas Bauernhansl. Overview of the state of the art in the production process of automotive wire harnesses, current research and future trends. *Procedia CIRP*, 81:387–392, 2019. 52nd CIRP Conference on Manufacturing Systems (CMS), Ljubljana, Slovenia, June 12-14, 2019.

[38] Kai Sheng Tai, Richard Socher, and Christopher D. Manning. Improved semantic representations from tree-structured long short-term memory networks, 2015.

[39] Jonathan Michaux, Patrick Holmes, Bohao Zhang, Che Chen, Baiyue Wang, Shrey Sahgal, Tiancheng Zhang, Sidhartha Dey, Shreyas Kousik, and Ram Vasudevan. Can't touch this: Real-time, safe motion planning and control for manipulators under uncertainty. *arXiv preprint arXiv:2301.13308*, 2023.

[40] Andrew Choi, Dezhong Tong, Mohammad K. Jawed, and Jungseock Joo. Implicit Contact Model for Discrete Elastic Rods in Knot Tying. *Journal of Applied Mechanics*, 88(5):051010, 03 2021.

[41] Jonathan Michaux, Seth Isaacson, Challen Enninful Adu, Adam Li, Rahul Kashyap Swayampakula, Parker Ewen, Sean Rice, Katherine A Skinner, and Ram Vasudevan. Let's make a splan: Risk-aware trajectory optimization in a normalized gaussian splat. *arXiv preprint arXiv:2409.16915*, 2024.

APPENDIX

A. Proof of Theorem 1

To prove the theorem, we begin by introducing the curvature binormal and material curvature.

Material Curvatures: The curvature binormal $\kappa \mathbf{b}^i$ is traditionally used to represent the turning angle and axis between two consecutive edges:

$$\kappa \mathbf{b}^i = \frac{2 \mathbf{e}^{i-1} \times \mathbf{e}^i}{\|\mathbf{e}^{i-1}\|_2 \|\mathbf{e}^i\|_2 + \mathbf{e}^{i-1} \cdot \mathbf{e}^i}, \quad (27)$$

where \mathbf{e}^{i-1} and \mathbf{e}^i are consecutive edge vectors, \times denotes the cross product, and \cdot denotes the dot product. By incorporating the material frame (3) and (4), the curvature binormal (27) is projected onto the material frame to quantify the extent to which the curvature aligns with the frame's orientation. This projection, which we call the material curvature, provides additional insights into the deformation characteristics, allowing us to distinguish between bending and twisting behaviors within the material frame and is defined as:

$$\boldsymbol{\omega}^{(i,j)} = (\kappa \mathbf{b}^i \cdot \mathbf{m}_1^j, \kappa \mathbf{b}^i \cdot \mathbf{m}_2^j)^T \quad \text{for } j \in \{i-1, i\}. \quad (28)$$

Potential Energy: The potential energy is composed of the bending energy and twisting energy:

$$P(\Gamma(\mathbf{X}_t, \boldsymbol{\theta}_t), \boldsymbol{\alpha}) = P_{\text{bend}}(\Gamma(\mathbf{X}_t, \boldsymbol{\theta}_t), \boldsymbol{\alpha}) + P_{\text{twist}}(\Gamma(\mathbf{X}_t, \boldsymbol{\theta}_t), \boldsymbol{\alpha}), \quad (29)$$

where

$$P_{\text{bend}}(\Gamma(\mathbf{X}_t, \boldsymbol{\theta}_t), \boldsymbol{\alpha}) = \sum_{i=1}^{n-1} \sum_{j=i-1}^i \frac{1}{2} (\boldsymbol{\omega}^{(i,j)} - \bar{\boldsymbol{\omega}}^{(i,j)})^T \mathbf{B}^j (\boldsymbol{\omega}^{(i,j)} - \bar{\boldsymbol{\omega}}^{(i,j)}), \quad (30)$$

and

$$P_{\text{twist}}(\Gamma(\mathbf{X}_t, \boldsymbol{\theta}_t), \boldsymbol{\alpha}) = \sum_{i=1}^{n-1} \frac{1}{2} \beta^i (\theta^i - \theta^{i-1})^2, \quad (31)$$

where $\bar{\boldsymbol{\omega}}^{(i,j)}$ denotes the undeformed material curvature, which is calculated when the DLO is in a static state without any external or internal forces applied, and \mathbf{B} and β , are components of $\boldsymbol{\alpha}$, representing the bending stiffness and twisting stiffness, respectively.

Gradient of Potential Energy: With (30) and (31), the gradient of (29) can be derived as following:

$$\begin{aligned} \frac{\partial P(\Gamma(\mathbf{X}_t, \boldsymbol{\theta}_t), \boldsymbol{\alpha})}{\partial \theta^i} &= \frac{\partial P_{\text{bend}}(\Gamma(\mathbf{X}_t, \boldsymbol{\theta}_t), \boldsymbol{\alpha})}{\partial \theta^i} + \\ &\quad \frac{\partial P_{\text{twist}}(\Gamma(\mathbf{X}_t, \boldsymbol{\theta}_t), \boldsymbol{\alpha})}{\partial \theta^i} \end{aligned} \quad (32)$$

We begin by deriving the first term. Note that θ^i is only relevant in $\boldsymbol{\omega}^{(i,i)}$ and $\boldsymbol{\omega}^{(i+1,i)}$. Using the chain rule, we obtain:

$$\frac{\partial P_{\text{bend}}(\Gamma(\mathbf{X}_t, \boldsymbol{\theta}_t), \boldsymbol{\alpha})}{\partial \theta^i} = \sum_{k=i}^{i+1} \frac{\partial P_{\text{bend}}(\Gamma(\mathbf{X}_t, \boldsymbol{\theta}_t), \boldsymbol{\alpha})}{\partial \boldsymbol{\omega}^{(k,i)}} \frac{\partial \boldsymbol{\omega}^{(k,i)}}{\partial \theta^i}. \quad (33)$$

To compute $\frac{\partial \boldsymbol{\omega}^{(k,i)}}{\partial \theta^i}$, we use the identities $\frac{\partial \mathbf{m}_1^i}{\partial \theta^i} = \mathbf{m}_2^i$ and

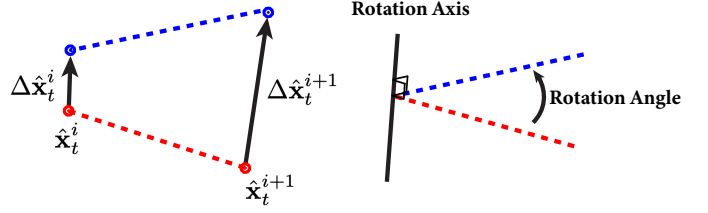


Fig. 10: An illustration of $\hat{\Omega}_\Delta^i(\hat{\mathbf{X}}, \Delta\hat{\mathbf{X}})$

$\frac{\partial \mathbf{m}_2^i}{\partial \theta^i} = -\mathbf{m}_1^i$. These lead to:

$$\frac{\partial \boldsymbol{\omega}^{(k,i)}}{\partial \theta^i} = \begin{bmatrix} 0 & 1 \\ -1 & 0 \end{bmatrix} \boldsymbol{\omega}^{(k,i)} \quad (34)$$

Substituting this result back, we obtain:

$$\begin{aligned} \frac{\partial P_{\text{bend}}(\Gamma(\mathbf{X}_t, \boldsymbol{\theta}_t), \boldsymbol{\alpha})}{\partial \theta^i} &= \sum_{k=i}^{i+1} (\mathbf{B}^k (\boldsymbol{\omega}^{(k,i)} - \bar{\boldsymbol{\omega}}^{(k,i)}))^T \cdot \\ &\quad \begin{bmatrix} 0 & 1 \\ -1 & 0 \end{bmatrix} \boldsymbol{\omega}^{(k,i)}, \end{aligned} \quad (35)$$

The second term of (32) can be derived, resulting in:

$$\frac{\partial P_{\text{twist}}(\Gamma(\mathbf{X}_t, \boldsymbol{\theta}_t), \boldsymbol{\alpha})}{\partial \theta^i} = \beta^i (\theta^i - \theta^{i-1}) - \beta^{i+1} (\theta^{i+1} - \theta^i) \quad (36)$$

By substituting (35) and (36) into (32), we obtain the analytical gradient of the potential energy.

B. Definition of $\hat{\Omega}_{\Delta,t}^i(\hat{\mathbf{X}}, \Delta\hat{\mathbf{X}})$ and $\hat{\Omega}^i$

In practice, it can be both challenging and impractical to attach hardware onto each segment for tracking its orientation changes. To address this limitation, we approximate the change in orientation, as illustrated in Figure 10. We define $\hat{\Omega}_\Delta^i(\hat{\mathbf{X}}, \Delta\hat{\mathbf{X}})$ as follows:

$$\hat{\Omega}_\Delta^i(\hat{\mathbf{X}}, \Delta\hat{\mathbf{X}}) = \frac{\hat{\mathbf{x}}^{i+1} - \hat{\mathbf{x}}^i}{\|\hat{\mathbf{x}}^{i+1} - \hat{\mathbf{x}}^i\|_2} \times \frac{(\hat{\mathbf{x}}^{i+1} + \Delta\hat{\mathbf{x}}^{i+1}) - (\hat{\mathbf{x}}^i + \Delta\hat{\mathbf{x}}^i)}{\|(\hat{\mathbf{x}}^{i+1} + \Delta\hat{\mathbf{x}}^{i+1}) - (\hat{\mathbf{x}}^i + \Delta\hat{\mathbf{x}}^i)\|_2} \quad (37)$$

Intuitively, the cross product of each edge's tangent vector provides an approximation of the rotation axis and orientation change for the segment i . This approximation becomes more accurate when Δ_t is small.

Next, we describe how to compute $\hat{\Omega}^i$. Note that it is defined recursively using the computation at the previous time step. As a result just within this appendix, we add a subscript t to the symbol. To compute $\hat{\Omega}_{t+1}^i$, we first convert both $\hat{\Omega}_t^i$ and the correction rotation $\hat{\Omega}_\Delta^i(\hat{\mathbf{X}}_t, \Delta\hat{\mathbf{X}}_t)$ from angle-axis to quaternions. We then update $\hat{\Omega}_t^i$ by applying $\hat{\Omega}_\Delta^i(\hat{\mathbf{X}}_t, \Delta\hat{\mathbf{X}}_t)$ in quaternion form, and finally convert the result back to angle-axis coordinates to obtain $\hat{\Omega}_{t+1}^i$. Note that we do not continuously use quaternions because angle-axis is more convenient for representing angular momentum.

C. Proof of Theorem 3

To prove Theorem 3, we first formulate the optimization problem:

$$\min_{\Delta\hat{\mathbf{X}}} \frac{1}{2} \left(C_A^{p,i}(\hat{\mathbf{X}}, \Delta\hat{\mathbf{X}}) \right)^2 \quad (38)$$

$$\text{s.t. } \Delta\hat{\mathbf{x}}^j = \mathbf{0}, \quad \forall j \{(p, i), (c, 1)\} \quad (39)$$

$$\mathbf{M}^{p,i} \Delta\hat{\mathbf{x}}^{p,i} + \mathbf{M}^{c,1} \Delta\hat{\mathbf{x}}^{c,1} = \mathbf{0}, \quad (40)$$

$$\mathbf{I}^{p,i} \hat{\Omega}_{\Delta}^{p,i}(\hat{\mathbf{X}}, \Delta\hat{\mathbf{X}}) = \mathbf{0}, \quad (41)$$

To solve the above optimization, we introduce Lagrange multipliers $\lambda_l \in \mathbb{R}^3$ and $\lambda_r \in \mathbb{R}^3$ associated with constraints (40) and (41), respectively. The corresponding Lagrangian \mathcal{L} can be found as follow:

$$\begin{aligned} \mathcal{L}(\Delta\hat{\mathbf{x}}^{p,i}, \Delta\hat{\mathbf{x}}^{c,1}, \lambda_l, \lambda_r) = & \\ & \frac{1}{2} \left(C_A^{p,i}(\hat{\mathbf{X}}, \Delta\hat{\mathbf{X}}) \right)^2 - \\ & \lambda_l^T (\mathbf{M}^i \Delta\hat{\mathbf{x}}^{p,i} + \mathbf{M}^{c,1} \Delta\hat{\mathbf{x}}^{c,1}) - \\ & \lambda_r^T \mathbf{I}^{p,i} \hat{\Omega}_{\Delta}^{p,i}(\hat{\mathbf{X}}, \Delta\hat{\mathbf{X}}) \end{aligned} \quad (42)$$

Next, we take the partial derivatives of (42) with respect to $\Delta\hat{\mathbf{x}}^{p,i}, \Delta\hat{\mathbf{x}}^{c,1}, \lambda_l, \lambda_r$. Setting each derivative to zero yields the system of equations (43), (44), (45), and (46).

$$\begin{aligned} \frac{\partial \mathcal{L}(\Delta\hat{\mathbf{x}}^{p,i}, \Delta\hat{\mathbf{x}}^{c,1}, \lambda_l, \lambda_r)}{\partial \Delta\hat{\mathbf{x}}^{p,i}} = & \\ C_A^{p,i}(\hat{\mathbf{X}}, \Delta\hat{\mathbf{X}}) \frac{(\hat{\mathbf{x}}^{p,i} + \Delta\hat{\mathbf{x}}^{p,i}) - (\hat{\mathbf{x}}^{c,1} + \Delta\hat{\mathbf{x}}^{c,1})}{\|(\hat{\mathbf{x}}^{p,i} + \Delta\hat{\mathbf{x}}^{p,i}) - (\hat{\mathbf{x}}^{c,1} + \Delta\hat{\mathbf{x}}^{c,1})\|_2} - & (43) \\ \lambda_l^T \mathbf{M}^{p,i} - \frac{\partial \lambda_r^T \mathbf{I}^{p,i} \hat{\Omega}_{\Delta}^{p,i}(\hat{\mathbf{X}}, \Delta\hat{\mathbf{X}})}{\partial \Delta\hat{\mathbf{x}}^{p,i}} = \mathbf{0} & \end{aligned}$$

$$\begin{aligned} \frac{\partial \mathcal{L}(\Delta\hat{\mathbf{x}}^{p,i}, \Delta\hat{\mathbf{x}}^{c,1}, \lambda_l, \lambda_r)}{\partial \Delta\hat{\mathbf{x}}^{c,1}} = & \\ C_A^{p,i}(\hat{\mathbf{X}}, \Delta\hat{\mathbf{X}}) \frac{(\hat{\mathbf{x}}^{c,1} + \Delta\hat{\mathbf{x}}^{c,1}) - (\hat{\mathbf{x}}^{p,i} + \Delta\hat{\mathbf{x}}^{p,i})}{\|(\hat{\mathbf{x}}^{p,i} + \Delta\hat{\mathbf{x}}^{p,i}) - (\hat{\mathbf{x}}^{c,1} + \Delta\hat{\mathbf{x}}^{c,1})\|_2} - & (44) \\ \lambda_l^T \mathbf{M}^{c,1} - \frac{\partial \lambda_r^T \mathbf{I}^{p,i} \hat{\Omega}_{\Delta}^{p,i}(\hat{\mathbf{X}}, \Delta\hat{\mathbf{X}})}{\partial \Delta\hat{\mathbf{x}}^{c,1}} = \mathbf{0} & \end{aligned}$$

$$\frac{\partial \mathcal{L}(\Delta\hat{\mathbf{x}}^{p,i}, \Delta\hat{\mathbf{x}}^{c,1}, \lambda_l, \lambda_r)}{\partial \lambda_l} = -(\mathbf{M}^i \Delta\hat{\mathbf{x}}^{p,i} + \mathbf{M}^{c,1} \Delta\hat{\mathbf{x}}^{c,1}) = \mathbf{0} \quad (45)$$

$$\frac{\partial \mathcal{L}(\Delta\hat{\mathbf{x}}^{p,i}, \Delta\hat{\mathbf{x}}^{c,1}, \lambda_l, \lambda_r)}{\partial \lambda_r} = -\mathbf{I}^i \lambda_r^T \mathbf{I}^{p,i} \hat{\Omega}_{\Delta}^{p,i}(\hat{\mathbf{X}}, \Delta\hat{\mathbf{X}}) = \mathbf{0} \quad (46)$$

We first observe that solving (45) leads to the following equation:

$$\Delta\hat{\mathbf{x}}^{c,1} = -(\mathbf{M}^{c,1})^{-1} \mathbf{M}^{p,i} \Delta\hat{\mathbf{x}}^{p,i} \quad (47)$$

This indicates that $\Delta\hat{\mathbf{x}}^{p,i}, \Delta\hat{\mathbf{x}}^{c,1}$ are colinear. Based on the definition of $\hat{\Omega}_{\Delta}^i(\hat{\mathbf{X}}, \Delta\hat{\mathbf{X}})$ in Appendix B, one can see that if $\Delta\hat{\mathbf{x}}^{p,i}, \Delta\hat{\mathbf{x}}^{c,1}$ are colinear, then $\hat{\Omega}_{\Delta}^{p,i}(\hat{\mathbf{X}}, \Delta\hat{\mathbf{X}}) = \mathbf{0}$. Note that this is true regardless of the size of Δ_t . Hence, it naturally satisfies (46). Next, summing (43) with (44) yields

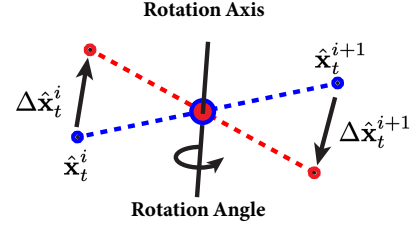


Fig. 11: An illustration of applying $\hat{\Omega}_{\Delta}^i$ to rotate the i -th segment.

the following:

$$\lambda_l \mathbf{M}^{p,i} + \lambda_r \mathbf{M}^{c,1} = \mathbf{0} \quad (48)$$

As mass matrices are always positive definite. This indicates $\lambda_l = \mathbf{0}$. Based on (43), (47) and (48), solving for $\Delta\hat{\mathbf{x}}^{p,i}$ is equivalent to solving the following equation:

$$C_A^{p,i}(\hat{\mathbf{X}}, \Delta\hat{\mathbf{X}}) = \mathbf{0} \quad (49)$$

After applying some algebraic manipulations, $\Delta\hat{\mathbf{x}}^{p,i}$ can be found to be:

$$\Delta\hat{\mathbf{x}}^{p,i} = \mathbf{M}^{c,1} (\mathbf{M}^{p,i} + \mathbf{M}^{c,1})^{-1} C_A^{p,i}(\hat{\mathbf{X}}, \mathbf{0}) \frac{(\hat{\mathbf{x}}^{c,1} - \hat{\mathbf{x}}^{p,i})}{\|(\hat{\mathbf{x}}^{c,1} - \hat{\mathbf{x}}^{p,i})\|_2},$$

Using $\Delta\hat{\mathbf{x}}^{p,i}$ and (47), one can find:

$$\Delta\hat{\mathbf{x}}^{c,1} = \mathbf{M}^{p,i} (\mathbf{M}^{p,i} + \mathbf{M}^{c,1})^{-1} C_A^{p,i}(\hat{\mathbf{X}}, \mathbf{0}) \frac{(\hat{\mathbf{x}}^{p,i} - \hat{\mathbf{x}}^{c,1})}{\|(\hat{\mathbf{x}}^{p,i} - \hat{\mathbf{x}}^{c,1})\|_2}.$$

D. Proof of Theorem 4

For convenience throughout this section, we suppress the arguments to functions for convenience. To prove Theorem 4, we begin by describing how $\hat{\Omega}_{\Delta}^i$ is applied to rotate the i -th segment. Note that Δ_t should be sufficiently small for $\hat{\Omega}_{\Delta}^i$ to accurately approximate the change in orientation. As shown in Figure 11, the rotation axis coincides with the center of the i -th segment. In practice, the rotation of the i -th segment is achieved by converting $\hat{\Omega}_{\Delta}^i$ into the rotation matrix $\hat{\Omega}_{\Delta}^i \mapsto \mathbf{R}_{\Delta}^i$. Consequently, we obtain $\Delta\hat{\mathbf{x}}^i$ and $\Delta\hat{\mathbf{x}}^{i+1}$ via

$$\Delta\hat{\mathbf{x}}^i = \mathbf{R}_{\Delta}^i \frac{(\hat{\mathbf{x}}^{i+1} - \hat{\mathbf{x}}^i)}{2}, \quad (50)$$

$$\Delta\hat{\mathbf{x}}^{i+1} = \mathbf{R}_{\Delta}^i \frac{(\hat{\mathbf{x}}^i - \hat{\mathbf{x}}^{i+1})}{2}. \quad (51)$$

Because each segment rotates only about its own center, linear momentum is naturally conserved. Thus, we can simplify the optimization problem and write the following optimization problem:

$$\min_{\Delta\hat{\mathbf{X}}} \frac{1}{2} \left(C_O^{p,i}(\hat{\mathbf{X}}, \Delta\hat{\mathbf{X}}) \right)^2 \quad (52)$$

$$\text{s.t. } \mathbf{I}^{p,i} \hat{\Omega}_{\Delta}^{p,i} + \mathbf{I}^{c,1} \hat{\Omega}_{\Delta}^{c,1} = \mathbf{0}, \quad (53)$$

where (25), (38), and (53) are analogous to (24), (38), and (40), respectively. Next, we introduce a Lagrange multiplier and follow the same derivation steps as in (43), (47), and (48),

which leads to:

$$\hat{\Omega}_{\Delta}^{p,i} = \mathbf{I}^{c,1} (\mathbf{I}^{c,1} + \mathbf{I}^{p,i})^{-1} C_O^{p,i}(\hat{\mathbf{X}}, \mathbf{0}) \frac{\hat{\Omega}^{c,1} - \hat{\Omega}^{p,i}}{\|\hat{\Omega}^{c,1} - \hat{\Omega}^{p,i}\|_2},$$

$$\hat{\Omega}_{\Delta}^{c,1} = \mathbf{I}^{p,i} (\mathbf{I}^{c,1} + \mathbf{I}^{p,i})^{-1} C_O^{p,i}(\hat{\mathbf{X}}, \mathbf{0}) \frac{\hat{\Omega}^{p,i} - \hat{\Omega}^{c,1}}{\|\hat{\Omega}^{c,1} - \hat{\Omega}^{p,i}\|_2}.$$

Once $\hat{\Omega}_{\Delta}^{p,i}$, $\hat{\Omega}_{\Delta}^{c,1}$ are obtained, (50) and (51) are used to update $\hat{\mathbf{x}}^{p,i}$ and $\hat{\mathbf{x}}^{c,1}$ accordingly.

E. ARMOUR

To address the shape matching task, we employ ARMOUR [39], an optimization-based framework for motion planning and control. The objective is to guide a robot arm so that it manipulates a BDLO from an initial configuration to a specified target configuration. ARMOUR accomplishes this through a receding-horizon approach: at each iteration, it solves an optimization problem to determine the robot's trajectory. ARMOUR parameterizes the robot's joint trajectories as polynomials, with polynomial coefficients serving as the decision variables. One end of the rope is rigidly attached to the robot's end effector, whose pose is determined by forward kinematics. By substituting the end effector's final pose into DEFT, we obtain a prediction of the rope's configuration at the conclusion of the motion. The optimization's cost function then minimizes the Euclidean distance between this predicted BDLO configuration from DEFT and the target configuration. To ensure the resultant motion is physically feasible, ARMOUR incorporates constraints on the robot's joint positions, velocities, and torques. Once the optimization is solved, the resulting trajectory is tracked by ARMOUR's controller. This planning-execution process is repeated until the rope achieves the desired configuration or a maximum iteration threshold is exceeded (in which case the task is deemed a failure). Additional details on ARMOUR's trajectory parameterization and its closed-loop controller can be found in [39, Section IX].